

---

# Plug-and-Play Diffusion Meets ADMM: Dual-Variable Coupling for Robust Medical Image Reconstruction

---

Chenhe Du<sup>1</sup> Xuanyu Tian<sup>1</sup> Qing Wu<sup>1</sup> Muyu Liu<sup>1</sup> Jingyi Yu<sup>1</sup> Hongjiang Wei<sup>2</sup> Yuyao Zhang<sup>1</sup>✉

## Abstract

Plug-and-Play diffusion prior (PnPDP) frameworks have emerged as a powerful paradigm for solving imaging inverse problems by treating pretrained generative models as modular priors. However, we identify a critical flaw in prevailing PnP solvers (e.g., based on HQS or Proximal Gradient): they function as *memoryless operators*, updating estimates solely based on instantaneous gradients. This lack of historical tracking inevitably leads to non-vanishing *steady-state bias*, where the reconstruction fails to strictly satisfy physical measurements under heavy corruption. To resolve this, we propose **Dual-Coupled PnP Diffusion**<sup>1</sup>, which restores the classical *dual variable* to provide integral feedback, theoretically guaranteeing asymptotic convergence to the exact data manifold. However, this rigorous geometric coupling introduces a secondary challenge: the accumulated dual residuals exhibit spectrally colored, structured artifacts that violate the Additive White Gaussian Noise (AWGN) assumption of diffusion priors, causing severe hallucinations. To bridge this gap, we introduce **Spectral Homogenization (SH)**, a frequency-domain adaptation mechanism that modulates these structured residuals into statistically compliant *pseudo-AWGN* inputs. This effectively aligns the solver’s rigorous optimization trajectory with the denoiser’s valid statistical manifold. Extensive experiments on CT and MRI reconstruction demonstrate that our approach resolves the bias-hallucination trade-off, achieving state-of-the-art fidelity with significantly accelerated convergence.

---

<sup>1</sup>ShanghaiTech University    <sup>2</sup>Shanghai Jiao Tong University.    Correspondence to: Yuyao Zhang <zhangyy8@shanghaitech.edu.cn>.

Preprint. February 27, 2026.

<sup>1</sup>Code is available at <https://github.com/duchenhe/DC-PnPDP>.

## 1. Introduction

Medical image reconstruction sits at the core of modern diagnostic workflows, bridging the gap between raw sensor data and clinical interpretation. In modalities such as Computed Tomography (CT) and Magnetic Resonance Imaging (MRI), physical constraints—ranging from reduced radiation dose to accelerated acquisition times—inevitably render the reconstruction task an ill-posed inverse problem. Mathematically, this is modeled as recovering a high-fidelity image  $\mathbf{x} \in \mathbb{R}^n$  from degraded measurements  $\mathbf{y}$ :

$$\mathbf{y} = \mathbf{A}\mathbf{x} + \mathbf{n}, \quad (1)$$

where  $\mathbf{A}$  denotes the forward operator (e.g., Radon transform or Fourier encoding) and  $\mathbf{n}$  represents measurement noise. To resolve the ill-posedness, one must introduce prior knowledge to restrict the solution space to valid anatomical manifolds. Modern approaches increasingly leverage Diffusion Models (Ho et al., 2020; Song et al., 2020) as learned priors. The prevailing paradigm, known as Plug-and-Play Diffusion Prior (PnPDP) (Zheng et al., 2025), decomposes the intractable posterior inference into two alternating sub-problems: a *data-consistency step* that enforces fidelity to  $\mathbf{y}$ , and a *prior step* that projects the estimate onto the data manifold using a pretrained diffusion model. This modularity has spurred a flurry of research: some works focus on designing more expressive diffusion backbones (enhancing the prior) (Karras et al., 2022; Dhariwal & Nichol, 2021; Rombach et al., 2022; Peebles & Xie, 2023), while others develop specialized solvers for the measurement operator (refining the likelihood) (Chung et al., 2022a; Wang et al., 2022; Song et al., 2021; Chung et al., 2022b; 2024; Zhu et al., 2023; Yang et al., 2024; Song et al., 2024; Du et al., 2024; Zhang et al., 2025).

Despite the empirical success of PnP diffusion, we identify a subtle yet critical flaw in current solvers (e.g., those based on Half-Quadratic Splitting (HQS) or Proximal Gradient methods): they are inherently *memoryless*. In each iteration, these algorithms update the solution based solely on the *instantaneous* gradient of the data-fidelity term. From a control theory perspective, they function as Proportional (P) controllers (Bequette, 2003). It is a well-established theoretical result that P-controllers cannot eliminate steady-

state bias when the system faces significant resistance (e.g., heavy measurement corruption or ill-conditioning). Consequently, current PnP solvers often converge to a biased equilibrium where the reconstruction fails to strictly satisfy the measurement constraints, effectively “compromising” between the physics and the prior. This limitation is particularly pernicious in medical imaging: unlike natural image synthesis where perceptual plausibility is paramount, diagnostic reconstruction demands rigorous fidelity to the observed measurements  $\mathbf{y}$ . A solver that settles for a “visually pleasing” approximation while violating physical constraints inherently compromises clinical reliability.

To eliminate this bias, classical optimization theory offers a rigorous solution: the *Dual Variable* (or Lagrange Multiplier). As exemplified in the Alternating Direction Method of Multipliers (ADMM) (Boyd et al., 2011), the dual variable acts as an integral memory, accumulating historical constraint violations over time to generate a corrective force. This mechanism theoretically guarantees that the solver converges to a strict consensus between the physical model and the regularization prior.

However, simply re-injecting this classical mechanism into modern diffusion loops proves practically non-trivial. We uncover a fundamental distributional conflict: the dual variable, by design, accumulates *structured* errors (e.g., directional streaks in CT or coherent aliasing in MRI) to correct the optimization trajectory. When these structured, spectrally colored residuals are fed back into the diffusion model (which is strictly trained on *Additive White Gaussian Noise*, AWGN), they constitute Out-of-Distribution (OOD) inputs. This mismatch causes the diffusion prior to misinterpretation of optimization artifacts as semantic content, leading to severe hallucinations or reconstruction divergence. This creates a fundamental geometric-statistical conflict: the dual variable is essential for the integral action in optimization, ensuring convergence, yet its structured spectral bias violates the i.i.d. Gaussian assumption of pretrained diffusion priors, leading to severe hallucination.

In this work, we propose a principled framework to resolve this conflict, termed **Dual-Coupled PnP Diffusion (DC-PnP)**. Our method bridges the gap between the rigorous geometry of ADMM and the statistical requirements of diffusion models. Instead of discarding the dual variable (as in current SOTA methods) or naively feeding it to the network (which causes OOD risks), we introduce a *Spectral Homogenization (SH)* mechanism. This module operates in the frequency domain to modulate the structured ADMM residuals, complementing them with synthetic noise to construct *Pseudo-AWGN* inputs on the fly. This allows the diffusion prior to operate within its valid statistical range while simultaneously preserving the dual-driven force essential for solving the optimization problem without bias. Our specific

contributions are:

- **Restoring the Dual Mechanism:** We re-introduce the explicit ADMM dual variable into the PnP diffusion loop, demonstrating that this “memory” term is essential for eliminating steady-state bias and ensuring robustness against heavy corruption.
- **Spectral Homogenization:** We propose a lightweight frequency-domain projection that transforms structured optimization residuals into spectrally whitened inputs. This effectively aligns the solver’s trajectory with the denoiser’s training distribution.
- **Efficiency and Performance:** Extensive experiments on Sparse-View CT and Accelerated MRI demonstrate that DC-PnP achieves superior convergence speed (approx.  $3\times$  faster than baselines) and reconstruction fidelity, establishing a new state-of-the-art (SOTA) for diffusion-based inverse solvers.

## 2. Background

### 2.1. Inverse Problems and Variational Formulation

We consider the generalized inverse problem of recovering an image  $\mathbf{x} \in \mathbb{R}^n$  from ill-posed measurements  $\mathbf{y} \in \mathbb{R}^m$ , governed by the linear model  $\mathbf{y} = \mathbf{A}\mathbf{x} + \mathbf{n}$ . A standard resolution strategy lies in the variational framework, which estimates  $\mathbf{x}$  by minimizing a composite objective:

$$\min_{\mathbf{x}} f(\mathbf{x}; \mathbf{y}) + \lambda \mathcal{R}(\mathbf{x}), \quad (2)$$

where  $f(\mathbf{x}; \mathbf{y}) = \frac{1}{2} \|\mathbf{A}\mathbf{x} - \mathbf{y}\|_{\mathbf{W}}^2$  enforces data consistency (weighted by noise precision  $\mathbf{W}$ ), and  $\mathcal{R}(\mathbf{x})$  is a regularization term encoding prior knowledge of the prior manifold.

### 2.2. ADMM and the Dual Variable Mechanism

To solve (2), the ADMM introduces an auxiliary variable  $\mathbf{z}$  to decouple the fidelity and prior terms:

$$\min_{\mathbf{x}, \mathbf{z}} f(\mathbf{x}) + \lambda \mathcal{R}(\mathbf{z}) \quad \text{s.t.} \quad \mathbf{x} = \mathbf{z}. \quad (3)$$

By forming the augmented Lagrangian, ADMM decomposes the problem into three iterative steps using a scaled dual variable  $\mathbf{u}$ :

$$\mathbf{x}^{(k+1)} = \arg \min_{\mathbf{x}} f(\mathbf{x}) + \frac{\rho}{2} \|\mathbf{x} - \mathbf{z}^{(k)} + \mathbf{u}^{(k)}\|_2^2, \quad (4)$$

$$\mathbf{z}^{(k+1)} = \text{prox}_{\frac{\lambda}{\rho} \mathcal{R}} \left( \mathbf{x}^{(k+1)} + \mathbf{u}^{(k)} \right), \quad (5)$$

$$\mathbf{u}^{(k+1)} = \mathbf{u}^{(k)} + \left( \mathbf{x}^{(k+1)} - \mathbf{z}^{(k+1)} \right). \quad (6)$$

Here,  $\rho > 0$  is a penalty parameter. Crucially, Eq. (6) reveals that  $\mathbf{u}^{(k)}$  acts as an integrator of the primal residual

$(\mathbf{x} - \mathbf{z})$ . In control theory terms, this provides *integral action*: it accumulates historical consensus errors to drive the system toward a theoretically rigorous fixed point where  $\mathbf{x}^* = \mathbf{z}^*$  and measurement constraints are strictly satisfied, eliminating steady-state bias.

### 2.3. Plug-and-Play Diffusion and the Statistical Gap

The core insight of plug-and-play (PnP) priors (Venkatakrishnan et al., 2013; Chan et al., 2016; Kamilov et al., 2023) is that the proximal operator in Eq.(5), formally defined as  $\text{prox}_{\tau\mathcal{R}}(\mathbf{v}) = \arg \min_{\mathbf{z}} \frac{1}{2}\|\mathbf{z} - \mathbf{v}\|_2^2 + \tau\mathcal{R}(\mathbf{z})$ , is mathematically equivalent to a maximum a posteriori (MAP) denoiser for AWGN. Consequently, PnP priors replace the explicit proximal operator in Eq. (5) with an off-the-shelf denoiser  $\mathcal{D}_\sigma$ . Modern PnP frameworks leverage Diffusion Models, where the denoiser  $\mathcal{D}_\sigma(\cdot)$  is formally linked to the score function of the data distribution  $p_{data}(\mathbf{x})$  via Tweedie’s formula (Robbins, 1992; Song et al., 2020):

$$\mathcal{D}_\sigma(\mathbf{v}) \approx \mathbf{v} + \sigma^2 \nabla_{\mathbf{v}} \log p_\sigma(\mathbf{v}) = \mathbb{E}[\mathbf{x}|\mathbf{v}]. \quad (7)$$

This substitution implies that the PnP iteration effectively performs Gradient Descent on the data fidelity term and Score Ascent on the prior.

**The Memoryless Approximation.** Most existing PnP diffusion solvers (Chung et al., 2022a; Zhu et al., 2023; Wu et al., 2024; Wang et al., 2024; Xu & Chi, 2024; Chu et al., 2025) typically adopt schemes akin to HQS, which effectively set  $u^{(k)} \equiv 0$ . While this reduces computational complexity, it discards the integral action of the dual variable, reducing the solver to a memoryless operator susceptible to asymptotic bias (as discussed in Sec. 1).

**The Distributional Conflict.** Reintroducing  $\mathbf{u}^{(k)}$  is non-trivial due to the statistical constraints of the denoiser. Pre-trained diffusion denoisers  $\mathcal{D}_\sigma$  rely on a strict AWGN Assumption: they provide a valid MAP estimate *if and only if* the input follows:

$$\mathbf{v} = \mathbf{x}_{\text{clean}} + \mathbf{n}, \quad \text{where } \mathbf{n} \sim \mathcal{N}(\mathbf{0}, \sigma^2 \mathbf{I}). \quad (8)$$

However, the ADMM dual-shifted input  $\mathbf{v}^{(k+1)} = \mathbf{x}^{(k+1)} + \mathbf{u}^{(k)}$  inherently contains structured, spatially correlated residuals (accumulated in  $\mathbf{u}$ ). This spectral coloring violates the AWGN assumption, pushing the input OOD and causing the diffusion model to hallucinate artifacts as semantic features.

## 3. Method: Dual-Coupled PnP Diffusion

We present **Dual-Coupled PnP Diffusion (DC-PnPDP)**, a framework designed to reconcile the rigorous convergence requirements of variational optimization with the statistical

rigidity of pretrained generative priors. Our core insight is to decouple the *geometric* and *statistical* roles of the solver: (1) We explicitly restore the ADMM dual variable to enforce asymptotic consensus (eliminating bias); (2) To prevent the resulting structured dual residuals from disrupting the denoiser, we introduce **Spectral Homogenization (SH)**, a frequency-domain adaptation module. SH transforms the colored optimization artifacts into statistically compliant pseudo-AWGN, ensuring the diffusion prior operates strictly within its valid training manifold.

### 3.1. The Dual-Coupled Iteration Scheme

We adopt the variable splitting formulation from Eq. (4)-(6). Unlike memoryless baselines that discard the dual history, we strictly maintain the dual state  $\mathbf{u}^{(k)}$  to track cumulative constraint violations. The overview iteration process, detailed in Algorithm 1, proceeds in two coupled phases:

**(1). Physics-Driven Update (Alg. 1, Step 1).** First, we solve the data-consistency sub-problem. Since  $f(\mathbf{x})$  is quadratic, this admits a closed-form solution or can be efficiently solved via Conjugate Gradient (CG):

$$\mathbf{x}^{(k+1)} = \arg \min_{\mathbf{x}} \|\mathbf{A}\mathbf{x} - \mathbf{y}\|_2^2 + \rho \|\mathbf{x} - (\mathbf{z}^{(k)} - \mathbf{u}^{(k)})\|_2^2. \quad (9)$$

**(2). The Dual-Shifted Interface (Alg. 1, Steps 2–4).**

To update the prior estimate  $\mathbf{z}$ , standard ADMM would compute the proximal operator on the dual-shifted variable  $\mathbf{v}^{(k+1)} := \mathbf{x}^{(k+1)} + \mathbf{u}^{(k)}$ . As analyzed in Sec. 2,  $\mathbf{v}^{(k+1)}$  is contaminated by spatially correlated, spectrally colored artifacts accumulated in  $\mathbf{u}^{(k)}$  (e.g., aliasing patterns). Direct application of the denoiser  $\mathcal{D}_\sigma(\mathbf{v}^{(k+1)})$  violates the AWGN assumption, leading to artifact hallucination. Therefore, we insert our distribution-correction module  $\mathcal{T}_{\text{SH}}$  before the denoiser:

$$\mathbf{z}^{(k+1)} = \mathcal{D}_\sigma \left( \mathcal{T}_{\text{SH}}(\mathbf{v}^{(k+1)}; \mathbf{z}^{(k)}) \right). \quad (10)$$

Finally, the dual variable is updated via  $\mathbf{u}^{(k+1)} = \mathbf{u}^{(k)} + (\mathbf{x}^{(k+1)} - \mathbf{z}^{(k+1)})$ , closing the feedback loop. Crucially, the stability of this rigorous feedback mechanism relies entirely on the denoiser accepting the dual-shifted input without exhibiting OOD behavior. In the following section, we detail how Spectral Homogenization  $\mathcal{T}_{\text{SH}}$  bridges this statistical gap by modulating the input’s frequency characteristics.

### 3.2. Spectral Homogenization (SH)

The goal of Spectral Homogenization is to construct a rectified input  $\tilde{\mathbf{v}}$  whose effective noise distribution matches the isotropic Gaussian statistics  $\mathcal{N}(\mathbf{0}, \sigma_t^2 \mathbf{I})$  expected by the diffusion model, without destroying the low-frequency semantic content of  $\mathbf{x}$ .

**Motivation: Why Frequency Domain Modulation?** The rationale for intervening in the frequency domain, rather than the spatial domain, stems from the need to balance *statistical whitening* with *structure preservation*. Physical artifacts (e.g., undersampling streaks or aliasing) are inherently *spectrally colored*, manifesting as energy concentrations in specific frequency bands, whereas the diffusion model expects a flat (white) spectrum. A naive spatial noise injection would degrade the entire image uniformly, destroying valid structural information. By contrast, operating in the frequency domain allows us to strictly enforce the AWGN energy profile by filling only the “spectral valleys” (missing energy) with synthetic noise, while preserving the “spectral peaks” (dominant energy) that correspond to the valid semantic guidance from the geometric update  $\mathbf{v}^{(k+1)}$ .

**Procedural Overview.** To realize this frequency-selective adaptation, the SH module  $\mathcal{T}_{\text{SH}}$  executes a three-stage process: (1) **Diagnosis:** We first estimate the Power Spectral Density (PSD) of the current optimization residuals to identify spectral deficits; (2) **Synthesis:** We construct a complementary noise field that is spectrally orthogonal to the artifacts yet statistically consistent with the target noise level; (3) **Fusion:** The synthetic noise is seamlessly merged with the dual-shifted input to produce a homogenized state  $\tilde{\mathbf{v}}^{(k+1)}$ . We detail these steps below.

**Step 1: Spectral Density Estimation of the Residual.** Since the ground truth noise realization within  $\mathbf{v}^{(k+1)}$  is inaccessible, we employ a *bootstrap* strategy to estimate the spectral deficit of the current iterate. We define the empirical residual field  $\mathbf{r}^{(k+1)}$  using the posterior mean estimate from the previous iteration,  $\mathbf{z}^{(k)}$ , as a proxy for the clean signal:

$$\mathbf{r}^{(k+1)} := \mathbf{v}^{(k+1)} - \mathbf{z}^{(k)}. \quad (11)$$

Intuitively,  $\mathbf{r}^{(k+1)}$  captures the structured deviations caused by the physics-based update and the dual accumulation.

Then we analyze the spectral characteristics of  $\mathbf{r}$  via its PSD, denoted as  $S_{\mathbf{r}}(\boldsymbol{\omega})$ . To mitigate variance, we formulate the PSD estimation as a non-parametric estimation problem. We compute the smoothed spectral estimate  $\hat{S}_{\mathbf{r}}$  via kernel density estimation in the frequency domain:

$$\hat{S}_{\mathbf{r}}(\boldsymbol{\omega}) := (|\mathcal{F}(\mathbf{r})(\boldsymbol{\omega})|^2) * \mathcal{K}_{\delta}, \quad (12)$$

where  $\mathcal{F}$  is the discrete Fourier transform,  $\mathcal{K}_{\delta}$  is a localized smoothing kernel with bandwidth  $\delta$ . This operation extracts the *spectral signature* of the solver-induced artifacts, identifying frequency bands where the dual variable accumulates excessive structured energy.

**Step 2: Complementary Noise Injection.** Our objective is to construct a rectified input  $\tilde{\mathbf{v}}$  whose effective noise

spectrum is theoretically flat at level  $\sigma^2$ . We define the *spectral deficit*  $\Delta S(\boldsymbol{\omega})$  as the gap between the target white spectrum and the current residual spectrum:

$$\Delta S(\boldsymbol{\omega}) := \max \left( \epsilon, \sigma^2(HW) - \hat{S}_{\mathbf{r}}(\boldsymbol{\omega}) \right), \quad (13)$$

where  $HW$  is the number of pixels and acts as the normalization factor for the unitary DFT, and  $\epsilon$  is a small constant for numerical stability.

To fill this deficit, we introduce a *complementary stochastic process*  $\boldsymbol{\xi}$ . Unlike standard additive noise,  $\boldsymbol{\xi}$  is constructed to be spectrally orthogonal to the dominant artifact modes. We synthesize  $\boldsymbol{\xi}$  by modulating a standard white Gaussian process  $\mathbf{n} \sim \mathcal{N}(\mathbf{0}, \mathbf{I})$ :

$$\boldsymbol{\xi}^{(k+1)} := \mathcal{F}^{-1} \left( \sqrt{\Delta S(\boldsymbol{\omega})} \odot e^{i\angle \mathcal{F}(\mathbf{n})} \right). \quad (14)$$

Here, the phase  $\angle \mathcal{F}(\mathbf{n})$  is taken from the random noise  $\mathbf{n}$ , ensuring spatial incoherence with the signal. While the amplitude is shaped by  $\Delta S(\boldsymbol{\omega})$ .

**Step 3: Fusion.** The final spectrally homogenized input to the denoiser is then formed as:

$$\tilde{\mathbf{v}}^{(k+1)} := \mathbf{v}^{(k+1)} + \boldsymbol{\xi}^{(k+1)}. \quad (15)$$

By construction, the effective noise in  $\tilde{\mathbf{v}}^{(k+1)}$  exhibits an approximately flat spectrum, mimicking the AWGN conditions  $\mathcal{D}_{\sigma}$  was trained on.

**Theoretical Justification: Moment Matching** The proposed  $\mathcal{T}_{\text{SH}}$  guarantees that the input to the diffusion model is statistically well-posed in terms of second-order moments. We formalize this via the following property.

**Proposition 3.1** (Second-Order Spectral Consistency). *Assume the injected phase is uniformly distributed and independent of  $\mathbf{r}$ . The expected Power Spectral Density of the homogenized effective noise  $\mathbf{n}_{\text{eff}} = \mathbf{r} + \boldsymbol{\xi}$  satisfies the whitening condition:*

$$\mathbb{E}_{\boldsymbol{\xi}} [S_{\mathbf{n}_{\text{eff}}}(\boldsymbol{\omega})] \approx \sigma^2(HW), \quad \forall \boldsymbol{\omega}. \quad (16)$$

*Consequently, the covariance matrix of the effective perturbation approximates a scaled identity matrix,  $\text{Cov}(\mathbf{n}_{\text{eff}}) \approx \sigma^2 \mathbf{I}$ , aligning with the AWGN assumption of  $\mathcal{D}_{\sigma}$ .*

**Remark 3.2.** This mechanism can be interpreted as **Coherence Breaking**. Physical artifacts are characterized by high spectral coherence (energy concentration) and phase correlation. By injecting the complementary process  $\boldsymbol{\xi}$ , we “drown out” the structured artifacts in specific frequency bands, effectively masking them as part of a global AWGN realization. This prevents the diffusion model from hallucinating structures based on artifact patterns.

**Algorithm 1** Dual-Coupled PnP Diffusion with Spectral Homogenization

---

```

1: Input: Measurements  $\mathbf{y}$ , Forward Operator  $\mathbf{A}$ , Pre-
   trained Diffusion Denoiser  $\mathcal{D}_\theta$ , Total Iterations  $K$ ,
   Noise Schedule  $\{\sigma_t\}_{t=1}^T$ .
2: Initialize:  $\mathbf{x}^{(0)}, \mathbf{z}^{(0)} \sim \mathcal{N}(\mathbf{0}, \mathbf{I})$ ,  $\mathbf{u}^{(0)} \leftarrow \mathbf{0}$ .
3: for  $k = 0$  to  $K - 1$  do
4:   // Set diffusion noise schedule
5:    $t \leftarrow t_k$  (e.g., linear spacing from  $T$  to 1)
6:   ▷ 1. Data Fidelity Optimization
7:    $\mathbf{x}^{(k+1)} \leftarrow \arg \min_{\mathbf{x}} \|\mathbf{A}\mathbf{x} - \mathbf{y}\|_2^2 + \lambda \|\mathbf{x} - \mathbf{z}^{(k)} + \mathbf{u}^{(k)}\|_2^2$ 
8:   ▷ 2. Spectral Homogenization
9:    $\mathbf{v}^{(k+1)} \leftarrow \mathbf{x}^{(k+1)} + \mathbf{u}^{(k)}$ 
10:   $\tilde{\mathbf{v}}^{(k+1)} \leftarrow \text{SpectralHomogenize}(\mathbf{v}^{(k+1)}, \mathbf{z}^{(k)}; \sigma_t)$ 
11:  ▷ 3. Denoising Prediction
12:   $\mathbf{z}^{(k+1)} \leftarrow \mathcal{D}_\theta(\tilde{\mathbf{v}}^{(k+1)}, t)$ 
13:  ▷ 4. Dual Variable Update
14:   $\mathbf{u}^{(k+1)} \leftarrow \mathbf{u}^{(k)} + (\mathbf{x}^{(k+1)} - \mathbf{z}^{(k+1)})$ 
15: end for
16: Return  $\mathbf{z}^{(K)}$ 

```

---

## 4. Experiments

In this section, we validate the effectiveness of the proposed DC-PnPDP framework. Our experiments aim to answer two key questions: (1) Does the introduction of the dual variable mitigate steady-state bias and improve convergence under challenging ill-posed problems? (2) Does Spectral Homogenization successfully suppress the colored artifacts inherent to dual-driven updates, preventing denoiser hallucination?

We evaluate our method on three representative medical imaging inverse problems: (i) Sparse-View (SV) CT Reconstruction, (ii) Limited-Angle (LA) CT Reconstruction, and (iii) Accelerated MRI Reconstruction. Furthermore, we conduct comprehensive ablation studies to isolate the contributions of the Dual-Variable Coupling and Spectral Homogenization modules.

### 4.1. Experimental Settings

**CT Dataset & Pre-processing.** We utilize the AbdomenCT-1K dataset (Ma et al., 2022), which contains 1112 CT scans from 12 medical centers. We employ 104,534 slices from 219 patients for training the diffusion prior, reserving six distinct patients (2,894 slices) for evaluation. All slices are resized to  $256 \times 256$ . We use the `torch-radon`<sup>2</sup> library to simulate parallel-beam (PB) geometry. For Sparse-View CT, we uniformly sample 20 views from  $[0^\circ, 180^\circ]$ ; for Limited-Angle CT, we utilize a restricted angular range of  $[0^\circ, 90^\circ]$  with 90 views. *Detailed settings are provided in Appendix A.2.*

<sup>2</sup><https://github.com/carterbox/torch-radon>

**MRI Dataset & Pre-processing.** We conduct experiments on the fastMRI knee dataset (Zbontar et al., 2018). We utilize the test dataset provided by (Zhang et al., 2025), comprising 96 slices. The complex-valued images are cropped to  $320 \times 320$ . Crucially, we simulate single-coil acquisition to rigorously evaluate the method’s performance under extreme undersampling conditions where parallel imaging gains (from coil sensitivity maps) are unavailable. To simulate accelerated acquisition, we employ 1D equidistant Cartesian masks with acceleration factors of  $6\times$  and  $10\times$ . We choose this equidistant sampling pattern over random subsampling because it reflects realistic clinical deployment. More importantly, it generates highly coherent artifacts that are substantially more difficult to remove compared to the incoherent artifacts resulting from random sampling (Knoll et al., 2019). For the proposed Spectral Homogenization in the complex domain, we apply the frequency-domain modulation to the real and imaginary channels separately.

**Implementation Details.** We adopt the EDM framework (Karras et al., 2022) for training the diffusion prior. For CT task, we train the model from scratch on AbdomenCT-1K. For MRI task, we utilize the pre-trained checkpoints (trained on fastMRI knee data) provided by (Zheng et al., 2025). All PnPDP methods are evaluated with the same pre-trained diffusion prior and under an identical compute budget of 50 NFEs, ensuring a strictly controlled and fair comparison. All experiments are conducted on a single NVIDIA RTX 4090 GPU.

**Methods in Comparison & Metrics.** We compare DC-PnPDP against a comprehensive suite of baselines, categorized into: (1) Classical Methods: FBP (for CT) and Zero-filling (for MRI). (2) SOTA Diffusion Solvers: We select four representative PnPDP methods: DDNM (Wang et al., 2022), DDS (Chung et al., 2024), DiffPIR (Zhu et al., 2023), and the recent DAPS (Zhang et al., 2025). It is worth highlighting that *DiffPIR* can be mathematically formulated as a PnP-HQS framework, whereas our approach represents an ADMM framework. The structural difference lies strictly in the dual variable update and the proposed Spectral Homogenization. *To ensure a rigorous comparison, we align the data-consistency operator of our method exactly with that of DiffPIR.* This control ensures that any performance gain is exclusively maximizing the contribution of the dual-coupling mechanism and spectral homogenization module. *Detailed hyperparameter alignments are provided in Appendix A.3.* Quantitative evaluation employs Peak Signal-to-Noise Ratio (PSNR) and Structural Similarity (SSIM) for data fidelity, and Learned Perceptual Image Patch Similarity (LPIPS) (Zhang et al., 2018) for perceptual quality.

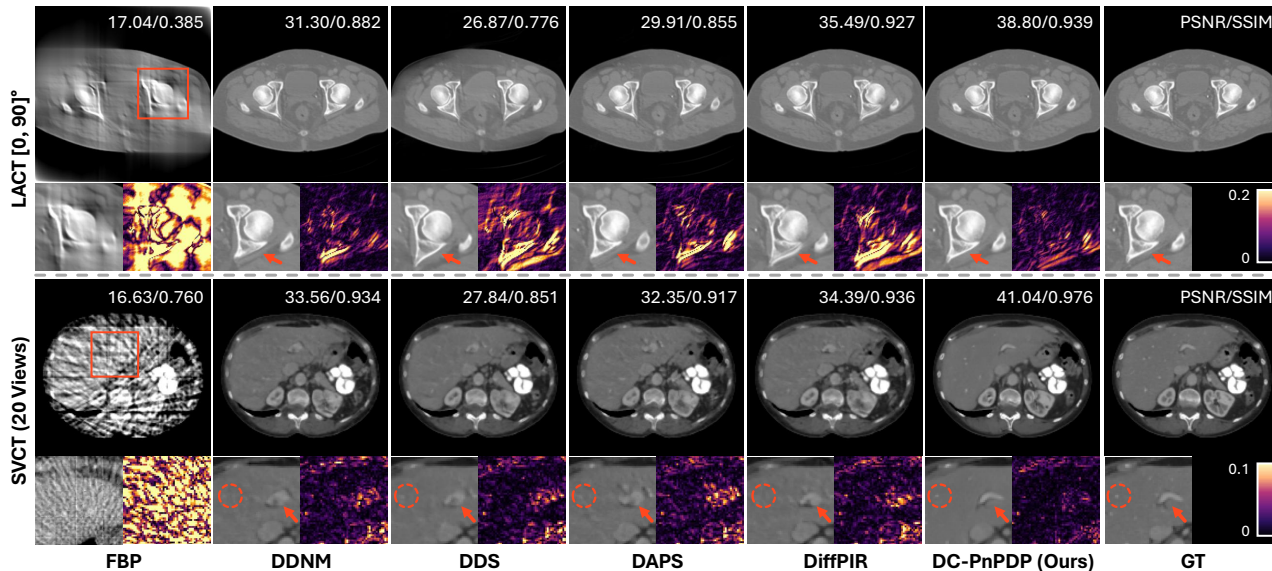


Figure 1. Qualitative comparisons on two CT reconstruction tasks. Visualization windows are set to  $[-800, 800]$  HU for LACT and  $[-175, 500]$  HU for SVCT, respectively.

Table 1. Quantitative results of compared method for different medical imaging tasks: SVCT of 20 views, LACT of  $[0, 90]^\circ$ , and accelerated MRI with acceleration factor (AF) is  $6\times$  and  $10\times$ . The best results are highlighted in **bold** and the second-best are underlined. Note that “ $A^\dagger y$ ” denotes the pseudo-inverse (FBP for CT, Zero-filling for MRI).

Method	LACT-90			SVCT-20			Accelerated MRI (AF=6)			Accelerated MRI (AF=10)		
	PSNR $\uparrow$	SSIM $\uparrow$	LPIPS $\downarrow$	PSNR $\uparrow$	SSIM $\uparrow$	LPIPS $\downarrow$	PSNR $\uparrow$	SSIM $\uparrow$	LPIPS $\downarrow$	PSNR $\uparrow$	SSIM $\uparrow$	LPIPS $\downarrow$
$A^\dagger y$	16.82	0.606	0.140	21.81	0.359	0.249	21.72	0.523	0.194	18.51	0.426	0.237
DDNM (Wang et al., 2022)	30.62	0.887	0.025	36.22	0.931	0.021	27.95	<u>0.763</u>	0.043	<u>25.32</u>	<u>0.681</u>	0.065
DDS (Chung et al., 2024)	24.86	0.775	0.056	<u>36.71</u>	<u>0.938</u>	0.021	27.12	0.737	<b>0.040</b>	24.01	0.644	<b>0.061</b>
DAPS (Zhang et al., 2025)	28.41	0.855	0.032	36.18	0.930	<u>0.020</u>	27.86	0.760	<u>0.042</u>	25.24	0.677	<u>0.062</u>
DiffPIR (Zhu et al., 2023)	<u>31.03</u>	<u>0.892</u>	<u>0.023</u>	36.23	0.931	0.021	<u>27.96</u>	<u>0.763</u>	0.043	25.27	0.680	0.065
DC-PnPDP (Ours)	<b>36.98</b>	<b>0.943</b>	<b>0.010</b>	<b>39.81</b>	<b>0.960</b>	<b>0.018</b>	<b>28.50</b>	<b>0.784</b>	0.046	<b>26.21</b>	<b>0.708</b>	0.066

## 4.2. Main Results

We present the quantitative comparison against SOTA PnP diffusion solvers in Table 1. Across all modalities and acceleration factors, the proposed **DC-PnPDP** consistently achieves the highest fidelity metrics (PSNR and SSIM).

**SVCT and LACT.** The advantages of our framework are most pronounced in the CT reconstruction tasks. In the challenging Limited-Angle (LACT-90) scenario, DC-PnPDP achieves a remarkable gain of **+5.95 dB** in PSNR compared to the strongest baseline, DiffPIR (36.98 dB vs. 31.03 dB). This empirical evidence strongly validates our theoretical analysis: current PnP methods (DiffPIR, DAPS) treat the data-consistency and prior sub-problems as loosely coupled steps. Functioning essentially as memoryless P-controllers, they lack the capacity to track the discrepancy between the likelihood and prior terms, often causing the optimization trajectory to stall with significant steady-state errors. In contrast, our dual-coupled mechanism acts as an Integral controller that strictly enforces the consensus constraint

( $x = z$ ), effectively eliminating the bias caused by the missing angular wedge. Similarly, in SVCT-20 task, our method outperforms the runner-up (DDS) by over **3 dB**, confirming that introducing the dual variable significantly enhances geometric accuracy even in less extreme settings.

Visual inspection of Figure 1 corroborates these quantitative gains. In the LACT task (top row), baselines such as DiffPIR and DAPS struggle to recover the bone structures within the missing wedge direction, resulting in severe blurring and streak artifacts (see zoomed-in ROI). Our DC-PnPDP, however, reconstructs sharp anatomical boundaries that are visually nearly identical to the GT. For the SVCT task (bottom row), we observe that memoryless baselines tend to *over-smooth* small low-contrast structures (e.g., the small lesion highlighted in the ROI). In contrast, our method preserves subtle tissue contrast and fine textures without hallucinating non-existent features. The error maps further highlight that DC-PnPDP yields the lowest pixel-wise reconstruction error, demonstrating superior fidelity across the entire field of view.

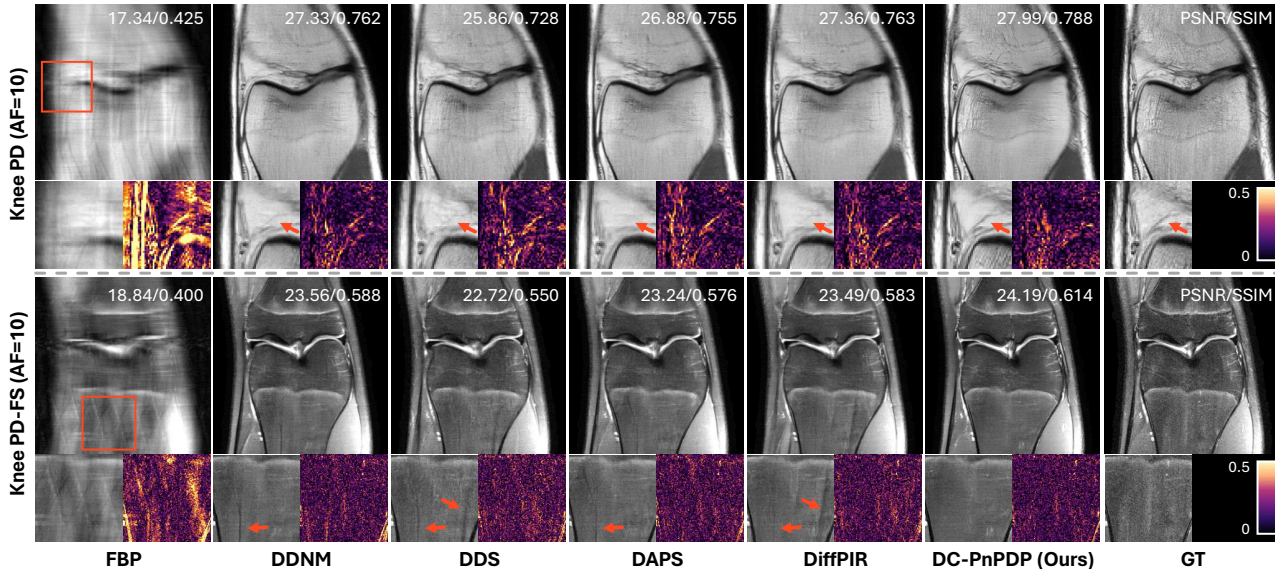


Figure 2. Qualitative comparisons of accelerated MRI (AF = 10) on knee proton density (PD) and proton density fat-suppressed (PD-FS) scans. Red arrows highlight major improvements and remaining aliasing artifacts.

**Accelerated MRI.** For MRI task, DC-PnPDP demonstrates superior robustness, particularly in the extreme  $10\times$  acceleration regime where it surpasses the runner-up (DAPS) by nearly 1 dB (26.21 dB vs. 25.24 dB). While LPIPS scores are comparable, our strictly superior PSNR/SSIM indicates a crucial trade-off: unlike pure diffusion baselines that often hallucinate non-existent high-frequency textures to satisfy perceptual metrics, our dual-constrained approach prioritizes physical fidelity. As shown in Figure 2, DC-PnPDP yields sharp, anatomically accurate boundaries and effectively eliminates the coherent vertical aliasing streaks (red arrows).

### 4.3. Ablation Study

**Effectiveness of Dual-Coupling & SH.** We verify the distinct roles of the proposed modules by progressively incorporating them into the framework. The quantitative results are summarized in Table 2. (1) The **Base PnP-HQS** configuration (mathematically equivalent to DiffPIR) yields the lowest fidelity (31.36 dB), confirming that memoryless controllers suffer from inherent steady-state bias. (2) Applying **SH Only** yields marginal gains (+0.15 dB). This result is structurally revealing: it confirms that the specific spectral pathology (colored artifacts) is primarily induced by the dual accumulation mechanism; in the absence of the dual variable, the distribution shift is less severe, rendering spectral correction less critical. (3) Conversely, reintroducing the **Dual Variable** drives the primary performance leap (+4.55 dB) by correcting the geometric bias, yet it still lags behind the full method by  $\sim 1.1$  dB due to the unmitigated spectral mismatch between the solver residuals and the denoiser’s

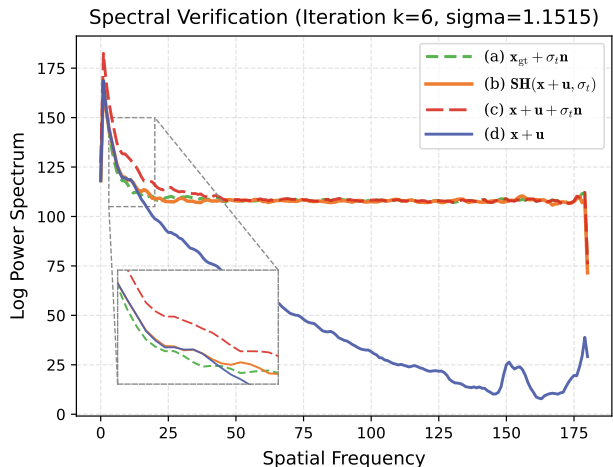
Table 2. **Component Ablation Study on LACT-90.** We validate the effectiveness of the proposed modules by progressively incorporating Dual-Coupling (DC) and Spectral Homogenization (SH). The baseline (Row 1) corresponds to a standard PnP-HQS solver (i.e., DiffPIR (Zhu et al., 2023)).

Components		Quantitative Metrics		
Dual Coupling (DC)	Spectral Homo. (SH)	PSNR $\uparrow$	SSIM $\uparrow$	LPIPS $\downarrow$
$\times$	$\times$	31.36	0.894	0.023
$\times$	$\checkmark$	31.51	0.898	0.022
$\checkmark$	$\times$	35.91	0.934	0.012
$\checkmark$	$\checkmark$	<b>37.02</b>	<b>0.943</b>	<b>0.011</b>

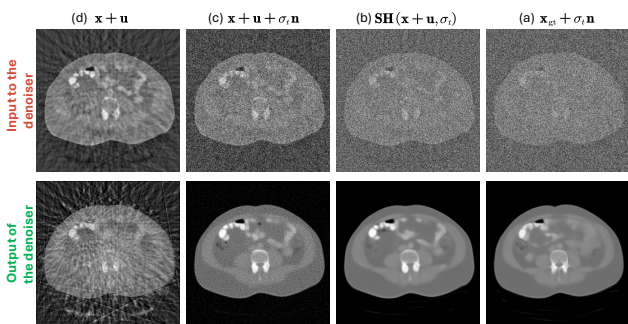
manifold. (4) Finally, the full **DC-PnPDP** achieves optimal performance (37.02 dB) by synergizing integral action (for geometric rigor) with spectral homogenization (for statistical alignment), effectively resolving the bias-hallucination trade-off.

### Effectiveness of Spectral Homogenization on Denoising.

To physically validate the mechanism of Spectral Homogenization, we analyze the frequency characteristics of the denoiser input. Figure 3 visualizes the spectral density and the corresponding single-step denoising output at an intermediate iteration. We identify two distinct failure modes in baselines: (1) The **raw dual input** (Line **d**, Blue) exhibits strong spectral coloring with high-frequency spikes, an OOD state that directly triggers artifact hallucination. (2) The **naive injection** strategy (Line **c**, Red) results in an *over-energized* spectrum (Red  $>$  Green). This creates a fundamental **variance mismatch** where the effective input noise exceeds the scheduled  $\sigma_t$ , causing the denoiser to under-correct and leave residual noise. In contrast, our



(a) **Spectral Analysis (PSD):** Visualizing the "Spectral Deficit".



(b) **Denoising Outcomes:** Comparison of denoiser inputs/outputs.

**Figure 3. Mechanism Verification: Why Spectral Homogenization Matters.** We analyze the spectral characteristics (**Top**) and the corresponding denoising outputs (**Bottom**) at iteration  $k = 6$ . **(a) Ideal Reference (Green):** The on-manifold input ( $x_{gt} + \sigma_t n$ ). **(b) Ours (Orange):** Our SH module aligns the spectrum perfectly, yielding clean results. **(c) Naive Injection (Red):** Adding noise ( $x + u + \sigma_t n$ ) creates an *over-energized* spectrum, leading to over-smoothing. **(d) No Injection (Blue):** The raw dual input ( $x + u$ ) causes OOD hallucinations.

**SH module**  $\mathcal{T}_{SH}$  (Line **b**, Orange) precisely fills the spectral deficits ("valleys") without overshooting. The resulting PSD perfectly aligns with the **ideal on-manifold reference** (Line **a**, Green), rendering the input statistically indistinguishable from the training distribution. Visual results confirm that this alignment successfully activates the optimal performance of the diffusion prior, yielding a clean restoration consistent with the ground truth.

**Convergence Speed & Computational Efficiency.** We evaluate the practical efficiency of our framework by analyzing the performance trajectory against NFE. Figure 4 plots the PSNR curves for both SVCT and LACT tasks. A striking observation is the superior convergence rate of DC-PnPDP (Red curves). Thanks to the integral action of the dual variable, which actively accumulates and corrects

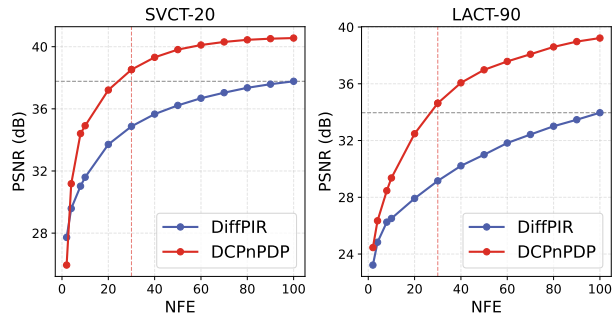


**Figure 4. Convergence Efficiency Analysis.** We compare the PSNR progression of DC-PnPDP (Red) vs. DiffPIR (Blue) over increasing NFE. Remarkably, DC-PnPDP achieves comparable or superior performance at just 30 steps than DiffPIR at 100 steps, demonstrating a  $\sim 3.3\times$  acceleration in inference efficiency.

residual errors, our method *quickly* navigates towards the optimal solution manifold. DC-PnPDP achieves a PSNR at **30 steps** that already surpasses the performance of DiffPIR at **100 steps** (indicated by the intersection of the red curve with the horizontal dashed line). This implies that our method can reduce the inference latency by approximately **3.3 $\times$**  without compromising image quality compared to the strongest baseline.

## 5. Conclusion and Discussion

In this work, we proposed **DC-PnP Diffusion**, a framework that pioneers the integration of the *dual variable*—a cornerstone of classical ADMM optimization—into the PnP diffusion paradigm. Our primary motivation was to bridge the gap between rigorous mathematical optimization and modern generative priors, injecting the proven convergence properties and geometric precision of traditional solvers into score-based reconstruction. We identified that this integration, while theoretically sound, is practically non-trivial: the reintroduction of the dual variable inevitably triggers structured spectral artifacts (OOD inputs) that disrupt the diffusion model. To resolve this, we proposed *Spectral Homogenization (SH)*, a tailored mechanism that adapts these dual-driven residuals into a statistically valid pseudo-white noise, thereby enabling the safe and effective utilization of the dual mechanism. Extensive experiments demonstrate that our approach achieves state-of-the-art fidelity and superior convergence efficiency.

Broadly, our work offers a new perspective on merging **traditional optimization wisdom** with **deep generative models**. We hope this framework serves as a stepping stone, encouraging future research to further explore how classical mathematical structures (e.g., integral action, momentum) can be revitalized to enhance the robustness of data-driven priors.

## References

- Bequette, B. W. *Process control: modeling, design, and simulation*. Prentice Hall Professional, 2003.
- Boyd, S., Parikh, N., Chu, E., Peleato, B., Eckstein, J., et al. Distributed optimization and statistical learning via the alternating direction method of multipliers. *Foundations and Trends® in Machine Learning*, 3(1):1–122, 2011.
- Chan, S. H., Wang, X., and Elgendy, O. A. Plug-and-play admm for image restoration: Fixed-point convergence and applications. *IEEE Transactions on Computational Imaging*, 3(1):84–98, 2016.
- Chu, W., Wu, Z., Chen, Y., Song, Y., and Yue, Y. Split gibbs discrete diffusion posterior sampling. *arXiv preprint arXiv:2503.01161*, 2025.
- Chung, H., Kim, J., Mccann, M. T., Klasky, M. L., and Ye, J. C. Diffusion posterior sampling for general noisy inverse problems. In *The Eleventh International Conference on Learning Representations*, 2022a.
- Chung, H., Sim, B., Ryu, D., and Ye, J. C. Improving diffusion models for inverse problems using manifold constraints. *Advances in Neural Information Processing Systems*, 35:25683–25696, 2022b.
- Chung, H., Lee, S., and Ye, J. C. Decomposed diffusion sampler for accelerating large-scale inverse problems. In *12th International Conference on Learning Representations, ICLR 2024*, 2024.
- Dhariwal, P. and Nichol, A. Diffusion models beat gans on image synthesis. *Advances in neural information processing systems*, 34:8780–8794, 2021.
- Du, C., Lin, X., Wu, Q., Tian, X., Su, Y., Luo, Z., Zheng, R., Chen, Y., Wei, H., Zhou, S. K., et al. Dper: Diffusion prior driven neural representation for limited angle and sparse view ct reconstruction. *arXiv preprint arXiv:2404.17890*, 2024.
- Ho, J., Jain, A., and Abbeel, P. Denoising diffusion probabilistic models. *Advances in neural information processing systems*, 33:6840–6851, 2020.
- Kamilov, U. S., Bouman, C. A., Buzzard, G. T., and Wohlberg, B. Plug-and-play methods for integrating physical and learned models in computational imaging: Theory, algorithms, and applications. *IEEE Signal Processing Magazine*, 40(1):85–97, 2023.
- Karras, T., Aittala, M., Aila, T., and Laine, S. Elucidating the design space of diffusion-based generative models. *Advances in Neural Information Processing Systems*, 35:26565–26577, 2022.
- Knoll, F., Hammernik, K., Kobler, E., Pock, T., Recht, M. P., and Sodickson, D. K. Assessment of the generalization of learned image reconstruction and the potential for transfer learning. *Magnetic resonance in medicine*, 81(1):116–128, 2019.
- Ma, J., Zhang, Y., Gu, S., Zhu, C., Ge, C., Zhang, Y., An, X., Wang, C., Wang, Q., Liu, X., Cao, S., Zhang, Q., Liu, S., Wang, Y., Li, Y., He, J., and Yang, X. Abdomenct-1k: Is abdominal organ segmentation a solved problem? *IEEE Transactions on Pattern Analysis and Machine Intelligence*, 44(10):6695–6714, 2022. doi:10.1109/TPAMI.2021.3100536.
- Peebles, W. and Xie, S. Scalable diffusion models with transformers. In *Proceedings of the IEEE/CVF international conference on computer vision*, pp. 4195–4205, 2023.
- Robbins, H. E. An empirical bayes approach to statistics. In *Breakthroughs in Statistics: Foundations and basic theory*, pp. 388–394. Springer, 1992.
- Rombach, R., Blattmann, A., Lorenz, D., Esser, P., and Ommer, B. High-resolution image synthesis with latent diffusion models. In *Proceedings of the IEEE/CVF conference on computer vision and pattern recognition*, pp. 10684–10695, 2022.
- Song, B., Kwon, S. M., Zhang, Z., Hu, X., Qu, Q., and Shen, L. Solving inverse problems with latent diffusion models via hard data consistency. In *ICLR*, 2024.
- Song, Y., Sohl-Dickstein, J., Kingma, D. P., Kumar, A., Ermon, S., and Poole, B. Score-based generative modeling through stochastic differential equations. *arXiv preprint arXiv:2011.13456*, 2020.
- Song, Y., Shen, L., Xing, L., and Ermon, S. Solving inverse problems in medical imaging with score-based generative models. In *International Conference on Learning Representations*, 2021.
- Venkatakrishnan, S. V., Bouman, C. A., and Wohlberg, B. Plug-and-play priors for model based reconstruction. In *2013 IEEE global conference on signal and information processing*, pp. 945–948. IEEE, 2013.
- Wang, H., Zhang, X., Li, T., Wan, Y., Chen, T., and Sun, J. Dmplug: A plug-in method for solving inverse problems with diffusion models. *Advances in Neural Information Processing Systems*, 37:117881–117916, 2024.
- Wang, Y., Yu, J., and Zhang, J. Zero-shot image restoration using denoising diffusion null-space model. In *The Eleventh International Conference on Learning Representations*, 2022.

- Wu, Z., Sun, Y., Chen, Y., Zhang, B., Yue, Y., and Bouman, K. L. Principled probabilistic imaging using diffusion models as plug-and-play priors. *Advances in Neural Information Processing Systems*, 37:118389–118427, 2024.
- Xu, X. and Chi, Y. Provably robust score-based diffusion posterior sampling for plug-and-play image reconstruction. *Advances in Neural Information Processing Systems*, 37:36148–36184, 2024.
- Yang, L., Ding, S., Cai, Y., Yu, J., Wang, J., and Shi, Y. Guidance with spherical gaussian constraint for conditional diffusion. In *International Conference on Machine Learning*, 2024.
- Zbontar, J., Knoll, F., Sriram, A., Murrell, T., Huang, Z., Muckley, M. J., Defazio, A., Stern, R., Johnson, P., Bruno, M., Parente, M., Geras, K. J., Katsnelson, J., Chandarana, H., Zhang, Z., Drozdal, M., Romero, A., Rabbat, M., Vincent, P., Yakubova, N., Pinkerton, J., Wang, D., Owens, E., Zitnick, C. L., Recht, M. P., Sodickson, D. K., and Lui, Y. W. fastMRI: An open dataset and benchmarks for accelerated MRI, 2018.
- Zhang, B., Chu, W., Berner, J., Meng, C., Anandkumar, A., and Song, Y. Improving diffusion inverse problem solving with decoupled noise annealing. In *Proceedings of the Computer Vision and Pattern Recognition Conference*, pp. 20895–20905, 2025.
- Zhang, R., Isola, P., Efros, A. A., Shechtman, E., and Wang, O. The unreasonable effectiveness of deep features as a perceptual metric. In *Proceedings of the IEEE conference on computer vision and pattern recognition*, pp. 586–595, 2018.
- Zheng, H., Chu, W., Zhang, B., Wu, Z., Wang, A., Feng, B., Zou, C., Sun, Y., Kovachki, N. B., Ross, Z. E., et al. Inversebench: Benchmarking plug-and-play diffusion priors for inverse problems in physical sciences. In *The Thirteenth International Conference on Learning Representations*, 2025.
- Zhu, Y., Zhang, K., Liang, J., Cao, J., Wen, B., Timofte, R., and Van Gool, L. Denoising diffusion models for plug-and-play image restoration. In *Proceedings of the IEEE/CVF Conference on Computer Vision and Pattern Recognition*, pp. 1219–1229, 2023.

## A. Appendix.

### A.1. Detailed Algorithm

---

**Algorithm 2** Detailed Implementation: Dual-Coupled PnP Diffusion
 

---

```

1: Input: Measurements  $\mathbf{y}$ , Forward Operator  $\mathbf{A}$ , Pre-trained Denoiser  $\mathcal{D}_\theta$ .
2: Hyperparameters:
3:   Total Iterations  $K$ , Penalty Parameter  $\lambda$ .
4:   Noise Schedule  $\{\sigma_t\}_{t=1}^T$  (aligned with denoiser training).
5:   SH Smoothing Kernel  $\mathcal{K}_w$  (e.g., Gaussian with window size  $w = 7$ ).
6: Initialize:  $\mathbf{x}^{(0)} \leftarrow \mathbf{A}^\top \mathbf{y}$ ,  $\mathbf{z}^{(0)} \sim \mathcal{N}(\mathbf{0}, \mathbf{I})$ ,  $\mathbf{u}^{(0)} \leftarrow \mathbf{0}$ .
7: // Begin Iterative Restoration
8: for  $k = 0$  to  $K - 1$  do
9:    $t \leftarrow t_k$  {Map iteration  $k$  to diffusion timestep}
10:  ▷ 1. Data Fidelity Optimization
11:   $\mathbf{x}^{(k+1)} \leftarrow \arg \min_{\mathbf{x}} \|\mathbf{A}\mathbf{x} - \mathbf{y}\|_2^2 + \lambda \|\mathbf{x} - \mathbf{z}^{(k)} + \mathbf{u}^{(k)}\|_2^2$ 
12:  ▷ 2. Spectral Homogenization
13:   $\mathbf{v}^{(k+1)} \leftarrow \mathbf{x}^{(k+1)} + \mathbf{u}^{(k)}$  {Dual-shifted input}
14:  // A. Spectral Density Estimation of the Residual
15:   $\mathbf{r} \leftarrow \mathbf{v}^{(k+1)} - \mathbf{z}^{(k)}$ 
16:   $\hat{S}_{\mathbf{r}} \leftarrow |\mathcal{F}(\mathbf{r})|^2 * \mathcal{K}_w$  {Smoothed Power Spectral Density}
17:  // B. Spectral Deficit Calculation (Clipping)
18:   $\Delta S \leftarrow \max\left(0, \sigma_t^2(HW) - \hat{S}_{\mathbf{r}}\right)$  {Target noise level  $\sigma_t$  varies with  $t$ }
19:  // C. Phase Transplantation (Ensures Hermitian Symmetry)
20:  Generate spatial white noise  $\mathbf{n} \sim \mathcal{N}(\mathbf{0}, \mathbf{I})$ 
21:   $\Phi \leftarrow \mathcal{F}(\mathbf{n}) \oslash |\mathcal{F}(\mathbf{n})|$  {Extract random phase structure}
22:   $\xi \leftarrow \mathcal{F}^{-1}\left(\sqrt{\Delta S} \odot \Phi\right)$  {Synthesize complementary noise}
23:  // D. Homogenized Input Construction
24:   $\tilde{\mathbf{v}}^{(k+1)} \leftarrow \mathbf{v}^{(k+1)} + \xi$ 
25:  ▷ 3. Denoising Prediction
26:   $\mathbf{z}^{(k+1)} \leftarrow \mathcal{D}_\theta(\tilde{\mathbf{v}}^{(k+1)}, t)$ 
27:  ▷ 4. Dual Variable Update
28:   $\mathbf{u}^{(k+1)} \leftarrow \mathbf{u}^{(k)} + (\mathbf{x}^{(k+1)} - \mathbf{z}^{(k+1)})$ 
29: end for
30: Return  $\mathbf{z}^{(K)}$ 

```

---

### A.2. Additional Details of Experiment

**CT Datasets & Pre-processing.** We utilize the **AbdomenCT-1K** dataset (Ma et al., 2022) for training and evaluation. To ensure high-quality priors, we strictly screen the dataset and select scans with a slice thickness of  $\leq 1$  mm. This screening process yields a subset of 225 high-resolution scans. We randomly reserve 6 scans for the test set and use the remaining 219 scans for training. Consistent with the main text, the Hounsfield Unit (HU) values are clipped to the range  $[-800, 800]$  and linearly normalized to  $[-1, 1]$ . For the parallel-beam simulation, we employ a 1D flat detector with 363 uniformly spaced bins and a detector pitch of 1.0 mm.

**Network Architecture & Training.** We adopt the EDM framework (Karras et al., 2022) for training the diffusion prior. The network architecture is a DDPM++ U-Net (Song et al., 2020) optimized for generating  $256 \times 256$  images. Training was conducted on a cluster of  $8 \times$  NVIDIA A100 (80GB) GPUs. We trained the model for approximately 35,000 steps (equivalent to  $\sim 37$  epochs) with a total batch size of 112. The entire training process took approximately 24 hours. We used the Adam optimizer with the following hyperparameters: learning rate  $lr = 1 \times 10^{-4}$ ,  $\beta_1 = 0.9$ ,  $\beta_2 = 0.999$ , and  $\epsilon = 10^{-8}$ .

### A.3. Implementation Details of Baselines

We provide detailed hyperparameter settings for all competing methods to ensure reproducibility.

**DDNM (Wang et al., 2022).** DDNM relies on a range-null space decomposition. The update rule can be expressed as

$$\mathbb{E}[\mathbf{x}_0 \mid \mathbf{x}_t, \mathbf{y}]^{(\text{DDNM})} \approx (\mathbf{I} - \mathbf{A}^\dagger \mathbf{A}) D_{\theta^*}(\mathbf{x}_t) + \mathbf{A}^\dagger \mathbf{y}, \quad (17)$$

where  $\mathbf{A}^\dagger$  denotes the pseudo-inverse of the measurement operator  $\mathbf{A}$ . For CT reconstruction,  $\mathbf{A}^\dagger$  is approximated using the Simultaneous Algebraic Reconstruction Technique (SIRT) to ensure stability. We set the number of SIRT iterations to 30 for all experiments.

**DDS (Chung et al., 2024).** DDS solves the proximal data-consistency sub-problem using the Conjugate Gradient (CG) method. We set the number of CG iterations to 5, which is followed the original paper and official implementation.

**DAPS (Zhang et al., 2025).** We utilize the official codebase for DAPS. The prior sampling step is implemented as a 1-step ODE solver (equivalent to Tweedie’s denoising formula). For the data-consistency step, we employ Langevin dynamics with 100 iterations to ensure sufficient exploration of the solution space.

**Controlled Comparison: DiffPIR (Zhu et al., 2023) vs. DC-PnPDP (Ours).** To rigorously isolate the contribution of our proposed modules, we formulate the comparison between DiffPIR (Zhu et al., 2023) and DC-PnP as a controlled ablation.

- **Formulation:** DiffPIR can be regarded as a standard **PnP-HQS** solver, while our DC-PnP is a **PnP-ADMM** solver.
- **Data Consistency (DC):** Both methods use the exact same Conjugate Gradient (CG) solver for the data-consistency sub-problem ( $\min_{\mathbf{x}} \|\mathbf{y} - \mathbf{A}\mathbf{x}\|^2 + \rho \|\mathbf{x} - \mathbf{v}\|^2$ ).
  - For **Sparse-View (SVCT)**, we set CG iterations = 20.
  - For **Limited-Angle (LACT)**, we set CG iterations = 100 and the proximal penalty parameter  $\rho = 1 \times 10^{-5} \times \frac{1}{\sigma_t^2}$ .
- **Key Difference:** Under this strictly controlled setting, the performance gap is exclusively attributed to two factors: (1) the update of the dual variable  $\mathbf{u}$  (present in ours, absent in DiffPIR), and (2) the noise injection strategy (Spectral Homogenization in ours vs. standard DDIM-style AWGN in DiffPIR).

## B. Justification of Spectral Residual Estimation via Bootstrapping

In Section 3.2, we approximate the true solver-induced residual using a bootstrap strategy, defined as  $\mathbf{r}^{(k+1)} = \mathbf{v}^{(k+1)} - \mathbf{z}^{(k)}$ . A natural concern is whether the estimation error in the pilot estimate  $\mathbf{z}^{(k)}$  (especially in early iterations) compromises the accuracy of the spectral diagnosis. Here, we provide a detailed analysis of why this approximation holds robustly in the context of inverse problems.

### B.1. Error Decomposition

Let  $\mathbf{x}_{\text{GT}}$  denote the ground truth image. The *true* solver residual containing the physics-based artifacts is  $\mathbf{r}_{\text{true}} = \mathbf{v}^{(k+1)} - \mathbf{x}_{\text{GT}}$ . Our empirical estimate  $\mathbf{r}^{(k+1)}$  can be decomposed as:

$$\begin{aligned} \mathbf{r}^{(k+1)} &= \mathbf{v}^{(k+1)} - \mathbf{z}^{(k)} \\ &= (\mathbf{v}^{(k+1)} - \mathbf{x}_{\text{GT}}) + (\mathbf{x}_{\text{GT}} - \mathbf{z}^{(k)}) \\ &= \underbrace{\mathbf{r}_{\text{true}}}_{\text{Structured Artifacts}} + \underbrace{\boldsymbol{\epsilon}_{\text{est}}}_{\text{Estimation Error}}, \end{aligned} \quad (18)$$

where  $\boldsymbol{\epsilon}_{\text{est}} = \mathbf{x}_{\text{GT}} - \mathbf{z}^{(k)}$  represents the denoising error of the previous step. The validity of our Spectral Homogenization relies on the condition that the spectral signature of  $\mathbf{r}_{\text{true}}$  is distinguishable from that of  $\boldsymbol{\epsilon}_{\text{est}}$ .

## B.2. Spectral Separability Analysis

We analyze the properties of these two terms in the frequency domain:

**1. Structured Artifacts ( $\mathbf{r}_{\text{true}}$ ): High Spectral Sparsity.** In ill-posed inverse problems, the artifacts in  $\mathbf{v}^{(k+1)}$  (derived from  $\mathbf{x}^{(k+1)} + \mathbf{u}^{(k)}$ ) are governed by the geometry of the forward operator  $\mathbf{A}$ .

- For **Sparse-View CT**, artifacts manifest as streaking patterns radiating from high-contrast regions. These correspond to energy concentration in a small set of angular frequency bands (a *sparse* support in Fourier space).
- For **Accelerated MRI**, artifacts manifest as periodic aliasing (Cartesian undersampling). This results in sharp, coherent peaks in the spectrum.

Mathematically, the PSD  $S_{\mathbf{r}_{\text{true}}}(\boldsymbol{\omega})$  exhibits high kurtosis, with energy concentrated in narrow bandwidths  $\Omega_{\text{art}}$ :

$$S_{\mathbf{r}_{\text{true}}}(\boldsymbol{\omega}) \gg 0, \quad \forall \boldsymbol{\omega} \in \Omega_{\text{art}}. \quad (19)$$

**2. Estimation Error ( $\epsilon_{\text{est}}$ ): Spectral Diffusion.** The term  $\epsilon_{\text{est}}$  represents the residual noise that the diffusion denoiser failed to remove or the details it failed to recover. Modern diffusion models (like DDPM/EDM) are trained to predict Gaussian noise. Consequently, their prediction errors tend to be incoherent and broadband (spectrally flat or slowly varying), lacking the strong geometric directionality of the physics artifacts. Thus,  $S_{\epsilon_{\text{est}}}(\boldsymbol{\omega})$  acts as a low-level, broadband background floor.

## B.3. The Dominance Condition

Spectral Homogenization effectively detects artifacts when the local Signal-to-Noise Ratio (SNR) in the frequency domain is high. Even if the total  $L_2$  error of the estimate is large (i.e.,  $\|\epsilon_{\text{est}}\|_2^2 \approx \|\mathbf{r}_{\text{true}}\|_2^2$ ), the peak energy density differs by orders of magnitude due to the energy compaction property of the artifacts:

$$\max_{\boldsymbol{\omega}} S_{\mathbf{r}_{\text{true}}}(\boldsymbol{\omega}) \gg \max_{\boldsymbol{\omega}} S_{\epsilon_{\text{est}}}(\boldsymbol{\omega}). \quad (20)$$

By computing the PSD, we effectively project the signal onto a basis where the artifacts are sparse and the error is dense. This allows the smoothing kernel  $\mathcal{K}_{\delta}$  (Eq. 12) to capture the envelope of the artifacts  $S_{\mathbf{r}_{\text{true}}}$  while averaging out the incoherent fluctuations of  $S_{\epsilon_{\text{est}}}$ . Therefore, the resulting mask  $\Delta S(\boldsymbol{\omega})$  correctly targets the artifacts without being significantly perturbed by the imperfections of  $\mathbf{z}^{(k)}$ .

## C. Fixed-Point Characterization and Bias Analysis

While establishing global convergence guarantees for non-convex PnP algorithms with stochastic diffusion priors remains an open theoretical challenge, we can rigorously analyze the properties of the algorithm's *fixed points*. This analysis reveals why the dual coupling is essential for unbiased reconstruction.

Let  $(\mathbf{x}^*, \mathbf{z}^*, \mathbf{u}^*)$  denote a fixed point of the iteration, assuming the spectral homogenization acts as a zero-mean perturbation in expectation at steady state.

**Theorem C.1** (Optimality of Dual-Coupled Fixed Points). *Assume the denoiser  $\mathcal{D}_{\sigma}$  acts as a proximal operator for some implicit regularizer  $\phi(\cdot)$ , i.e.,  $\mathcal{D}_{\sigma}(\mathbf{v}) = \text{prox}_{\gamma\phi}(\mathbf{v})$ . 1. The fixed point  $(\mathbf{x}^*, \mathbf{z}^*, \mathbf{u}^*)$  of the proposed Dual-Coupled PnP ADMM satisfies the first-order optimality condition of the original problem:*

$$\mathbf{0} \in \nabla f(\mathbf{x}^*) + \partial\phi(\mathbf{x}^*). \quad (21)$$

2. Conversely, a PnP scheme that discards the dual variable (setting  $\mathbf{u} \equiv \mathbf{0}$ ) converges to a biased solution  $\tilde{\mathbf{x}}$  satisfying:

$$\mathbf{0} \in \nabla f(\tilde{\mathbf{x}}) + \partial\phi(\tilde{\mathbf{x}}) + \underbrace{(\tilde{\mathbf{x}} - \mathcal{D}_{\sigma}(\tilde{\mathbf{x}}))}_{\text{Systematic Bias}}. \quad (22)$$

*Proof. Part 1 (Proposed Method):* At a fixed point,  $\mathbf{u}^{k+1} = \mathbf{u}^k$ , which implies  $\mathbf{x}^* - \mathbf{z}^* = \mathbf{0}$  via Eq. (6), ensuring consensus  $\mathbf{x}^* = \mathbf{z}^*$ . The x-update (4) implies  $\mathbf{0} = \nabla f(\mathbf{x}^*) + \rho(\mathbf{x}^* - \mathbf{z}^* + \mathbf{u}^*) \implies \nabla f(\mathbf{x}^*) = -\rho\mathbf{u}^*$ . The z-update (prior step)

implies  $\mathbf{z}^* = \text{prox}_{\gamma\phi}(\mathbf{x}^* + \mathbf{u}^*)$ . By definition of the proximal operator, this yields  $\mathbf{x}^* + \mathbf{u}^* - \mathbf{z}^* \in \gamma\partial\phi(\mathbf{z}^*)$ . Substituting  $\mathbf{x}^* = \mathbf{z}^*$ , we get  $\mathbf{u}^* \in \gamma\partial\phi(\mathbf{x}^*)$ . Combining these,  $\nabla f(\mathbf{x}^*) = -\rho\mathbf{u}^* \in -\rho\gamma\partial\phi(\mathbf{x}^*)$ . Setting parameters consistently recovers  $\mathbf{0} \in \nabla f + \partial\phi$ .

*Part 2 (Loose Coupling / No Dual):* If  $\mathbf{u}$  is omitted, the updates effectively become alternating minimization without memory. The  $\mathbf{x}$ -update becomes  $\nabla f(\tilde{\mathbf{x}}) + \rho(\tilde{\mathbf{x}} - \tilde{\mathbf{z}}) = 0$ . The  $\mathbf{z}$ -update becomes  $\tilde{\mathbf{z}} = \mathcal{D}_\sigma(\tilde{\mathbf{x}})$ . Substituting  $\tilde{\mathbf{z}}$ , we get  $\nabla f(\tilde{\mathbf{x}}) + \rho(\tilde{\mathbf{x}} - \mathcal{D}_\sigma(\tilde{\mathbf{x}})) = 0$ . The term  $\rho(\tilde{\mathbf{x}} - \mathcal{D}_\sigma(\tilde{\mathbf{x}}))$  represents the gradient of the prior  $\nabla\phi(\tilde{\mathbf{x}})$  *only if*  $\tilde{\mathbf{x}}$  is already a perfect denoised image. However, in practice,  $\tilde{\mathbf{x}}$  contains residual noise. The discrepancy leads to a non-vanishing gradient term, creating a permanent fixed-point bias where data consistency fights against the denoiser without the buffering capacity of the dual variable to absorb the residual.  $\square$

## D. Theoretical Analysis of Fixed-Point Properties

In this section, we provide a rigorous analysis of the fixed-point characterization of the proposed Dual-Coupled PnP framework. While establishing global convergence sequences for non-convex, stochastic PnP algorithms remains an open problem in the field, analyzing the *fixed points* (i.e., the steady states) of the algorithm provides critical insights into the correctness of the solution.

Specifically, we prove that the explicit inclusion of the dual variable enables the framework to converge to a stationary point of the original variational problem, whereas standard PnP methods (which omit the dual variable) suffer from a systematic bias.

### D.1. Preliminaries and Assumptions

We consider the composite optimization problem:

$$\min_{\mathbf{x}} f(\mathbf{x}) + \lambda\phi(\mathbf{x}), \quad (23)$$

where  $f(\mathbf{x}) = \frac{1}{2}\|\mathbf{A}\mathbf{x} - \mathbf{y}\|_{\mathbf{W}}^2$  is the data-fidelity term, and  $\phi(\mathbf{x})$  is an implicit regularizer induced by the image prior.

To connect the denoiser to the optimization objective, we adopt the standard assumption in PnP literature regarding the relationship between the denoiser and the proximal operator.

**Assumption D.1** (Denoiser as Proximal Operator). We assume that the pretrained denoiser  $\mathcal{D}_\sigma$  acts locally as the proximal operator of the regularizer  $\phi$  with parameter  $\gamma > 0$ :

$$\mathcal{D}_\sigma(\mathbf{v}) \approx \text{prox}_{\gamma\phi}(\mathbf{v}) \triangleq \arg \min_{\mathbf{z}} \left( \frac{1}{2}\|\mathbf{z} - \mathbf{v}\|_2^2 + \gamma\phi(\mathbf{z}) \right). \quad (24)$$

For diffusion models, this is motivated by Tweedie's formula, which links the MMSE denoiser to the score function  $\nabla \log p(\mathbf{x})$ .

### D.2. Theorem 1: Optimality of Dual-Coupled Fixed Points

**Theorem D.2.** *Let  $(\mathbf{x}^*, \mathbf{z}^*, \mathbf{u}^*)$  be a fixed point of the deterministic backbone of the proposed Dual-Coupled PnP ADMM iterations. Under Assumption D.1,  $\mathbf{x}^*$  satisfies the first-order optimality condition of the original problem (23) with effective regularization weight  $\lambda = \rho\gamma$ .*

*Proof.* The deterministic updates of our ADMM formulation are:

$$\mathbf{x}^{k+1} := \arg \min_{\mathbf{x}} f(\mathbf{x}) + \frac{\rho}{2}\|\mathbf{x} - \mathbf{z}^k + \mathbf{u}^k\|_2^2 \quad (25)$$

$$\mathbf{z}^{k+1} := \mathcal{D}_\sigma(\mathbf{x}^{k+1} + \mathbf{u}^k) \quad (26)$$

$$\mathbf{u}^{k+1} := \mathbf{u}^k + \mathbf{x}^{k+1} - \mathbf{z}^{k+1} \quad (27)$$

At a fixed point  $(\mathbf{x}^*, \mathbf{z}^*, \mathbf{u}^*)$ , we have  $\mathbf{x}^{k+1} = \mathbf{x}^k = \mathbf{x}^*$ , etc.

**Step 1: Consensus.** From the dual update (27), stationarity implies:

$$\mathbf{u}^* = \mathbf{u}^* + \mathbf{x}^* - \mathbf{z}^* \implies \mathbf{x}^* = \mathbf{z}^*. \quad (28)$$

Thus, the primal and auxiliary variables reach perfect consensus.

**Step 2: Data Consistency Condition.** From the x-update (25), the first-order optimality condition is:

$$\nabla f(\mathbf{x}^*) + \rho(\mathbf{x}^* - \mathbf{z}^* + \mathbf{u}^*) = \mathbf{0}. \quad (29)$$

Using the consensus property  $\mathbf{x}^* = \mathbf{z}^*$ , this simplifies to:

$$\nabla f(\mathbf{x}^*) + \rho\mathbf{u}^* = \mathbf{0} \implies \nabla f(\mathbf{x}^*) = -\rho\mathbf{u}^*. \quad (30)$$

This physically implies that the dual variable  $\mathbf{u}^*$  perfectly balances the gradient of the data-fidelity term.

**Step 3: Prior Condition.** From the z-update (26) and Assumption D.1:

$$\mathbf{z}^* = \text{prox}_{\gamma\phi}(\mathbf{x}^* + \mathbf{u}^*). \quad (31)$$

By the definition of the proximal operator,  $\mathbf{z}^*$  must satisfy:

$$\mathbf{0} \in (\mathbf{z}^* - (\mathbf{x}^* + \mathbf{u}^*)) + \gamma\partial\phi(\mathbf{z}^*). \quad (32)$$

Rearranging terms and utilizing  $\mathbf{x}^* = \mathbf{z}^*$ :

$$\mathbf{u}^* \in \gamma\partial\phi(\mathbf{x}^*). \quad (33)$$

**Step 4: Global Optimality.** Combining (30) and (33), we substitute  $\mathbf{u}^*$ :

$$\nabla f(\mathbf{x}^*) \in -\rho(\gamma\partial\phi(\mathbf{x}^*)) \implies \mathbf{0} \in \nabla f(\mathbf{x}^*) + \rho\gamma\partial\phi(\mathbf{x}^*). \quad (34)$$

Letting  $\lambda = \rho\gamma$ , this is exactly the optimality condition for  $\min f(\mathbf{x}) + \lambda\phi(\mathbf{x})$ .  $\square$

### D.3. Theorem 2: Systematic Bias in Loosely Coupled PnP

**Theorem D.3.** Consider a "Loose PnP" scheme that omits the dual variable (equivalent to setting  $\mathbf{u}^k \equiv \mathbf{0}$ ). Let  $\tilde{\mathbf{x}}$  be a fixed point of this scheme. Then  $\tilde{\mathbf{x}}$  satisfies a biased optimality condition:

$$\mathbf{0} \in \nabla f(\tilde{\mathbf{x}}) + \frac{\rho}{\sigma^2} \mathcal{E}_{bias}(\tilde{\mathbf{x}}), \quad (35)$$

where the bias term depends on the residual noise of the denoiser output.

*Proof.* Without the dual variable, the updates simplify to:

$$\tilde{\mathbf{x}} := \arg \min_{\mathbf{x}} f(\mathbf{x}) + \frac{\rho}{2} \|\mathbf{x} - \tilde{\mathbf{z}}\|_2^2 \quad (36)$$

$$\tilde{\mathbf{z}} := \mathcal{D}_\sigma(\tilde{\mathbf{x}}) \quad (37)$$

The x-update implies:

$$\nabla f(\tilde{\mathbf{x}}) + \rho(\tilde{\mathbf{x}} - \tilde{\mathbf{z}}) = \mathbf{0}. \quad (38)$$

Substituting  $\tilde{\mathbf{z}} = \mathcal{D}_\sigma(\tilde{\mathbf{x}})$ :

$$\nabla f(\tilde{\mathbf{x}}) + \rho(\tilde{\mathbf{x}} - \mathcal{D}_\sigma(\tilde{\mathbf{x}})) = \mathbf{0}. \quad (39)$$

Using Tweedie's formula approximation  $\mathcal{D}_\sigma(\mathbf{x}) \approx \mathbf{x} + \sigma^2 \nabla \log p(\mathbf{x})$ , the term in the parenthesis becomes:

$$\tilde{\mathbf{x}} - \mathcal{D}_\sigma(\tilde{\mathbf{x}}) \approx -\sigma^2 \nabla \log p(\tilde{\mathbf{x}}). \quad (40)$$

Superficially, substituting this into (39) yields  $\nabla f(\tilde{\mathbf{x}}) - \rho\sigma^2 \nabla \log p(\tilde{\mathbf{x}}) \approx \mathbf{0}$ , which resembles the MAP condition.

**However, a critical contradiction arises:** The diffusion denoiser  $\mathcal{D}_\sigma(\cdot)$  is trained to estimate  $\mathbf{x}_{clean}$  from a *noisy* input  $\mathbf{x}_{clean} + \mathbf{n}$ . In the loose PnP scheme, the input to the denoiser is  $\tilde{\mathbf{x}}$ , which is the current *clean* estimate of the image.

- If  $\tilde{\mathbf{x}}$  is truly clean and noise-free, an ideal denoiser acts as an identity map:  $\mathcal{D}_\sigma(\tilde{\mathbf{x}}) \approx \tilde{\mathbf{x}}$ . In this case, (39) becomes  $\nabla f(\tilde{\mathbf{x}}) \approx \mathbf{0}$ , meaning the prior is effectively ignored, and the solution collapses to the Maximum Likelihood Estimate (overfitting to noisy measurements).

- If  $\mathcal{D}_\sigma$  is not an identity map on clean data (which is true for real networks), it introduces a "hallucination error" or "texture smoothing" bias  $\mathcal{E}_{bias} = \tilde{\mathbf{x}} - \mathcal{D}_\sigma(\tilde{\mathbf{x}})$ . This term acts as a phantom force that does not correspond to the true score function of the prior distribution.

Consequently,  $\tilde{\mathbf{x}}$  is not a stationary point of  $f(\mathbf{x}) + \lambda\phi(\mathbf{x})$ , but rather a compromise point dictated by the denoiser's behavior on out-of-distribution (clean) inputs. □

#### **D.4. Physical Interpretation: The Role of Integral Action**

The contrast between Theorem 1 and Theorem 2 can be understood through a control theory analogy.

- *Current PnPDP (No Dual)* acts as a **Proportional (P) Controller**. It tries to reduce the error between the data-consistency term and the prior term simply by pulling them together ( $\rho(\mathbf{x} - \mathbf{z})$ ). Like any P-controller, it suffers from a "steady-state error" (bias) because a non-zero force (gradient) is required to maintain the balance between  $f$  and  $\phi$ .
- *Dual-Coupled PnPDP (Our Method)* acts as a **Proportional-Integral (PI) Controller**. The dual variable  $\mathbf{u}$  integrates the discrepancy  $(\mathbf{x} - \mathbf{z})$  over time. This integral action builds up a force that exactly cancels the gradient  $\nabla f(\mathbf{x}^*)$  at the optimal solution, allowing the error  $(\mathbf{x} - \mathbf{z})$  to settle to exactly zero. This ensures that the final result is physically consistent with both the measurements and the prior.

#### **E. Additional Visual Results**

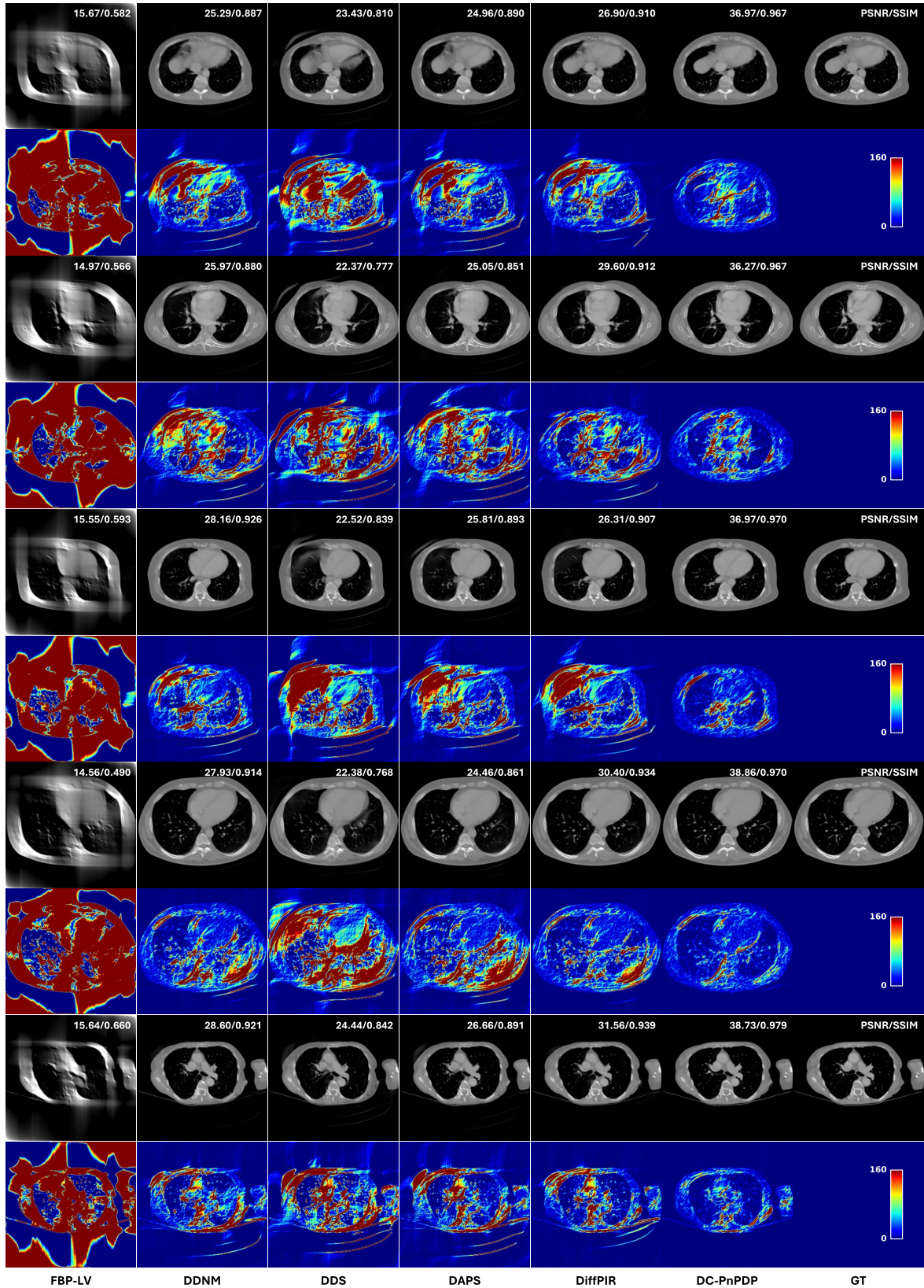


Figure 5. Qualitative comparisons on LACT of  $[0, 90]^\circ$  reconstruction tasks. Visualization windows are set to  $[-800, 800]$  HU.

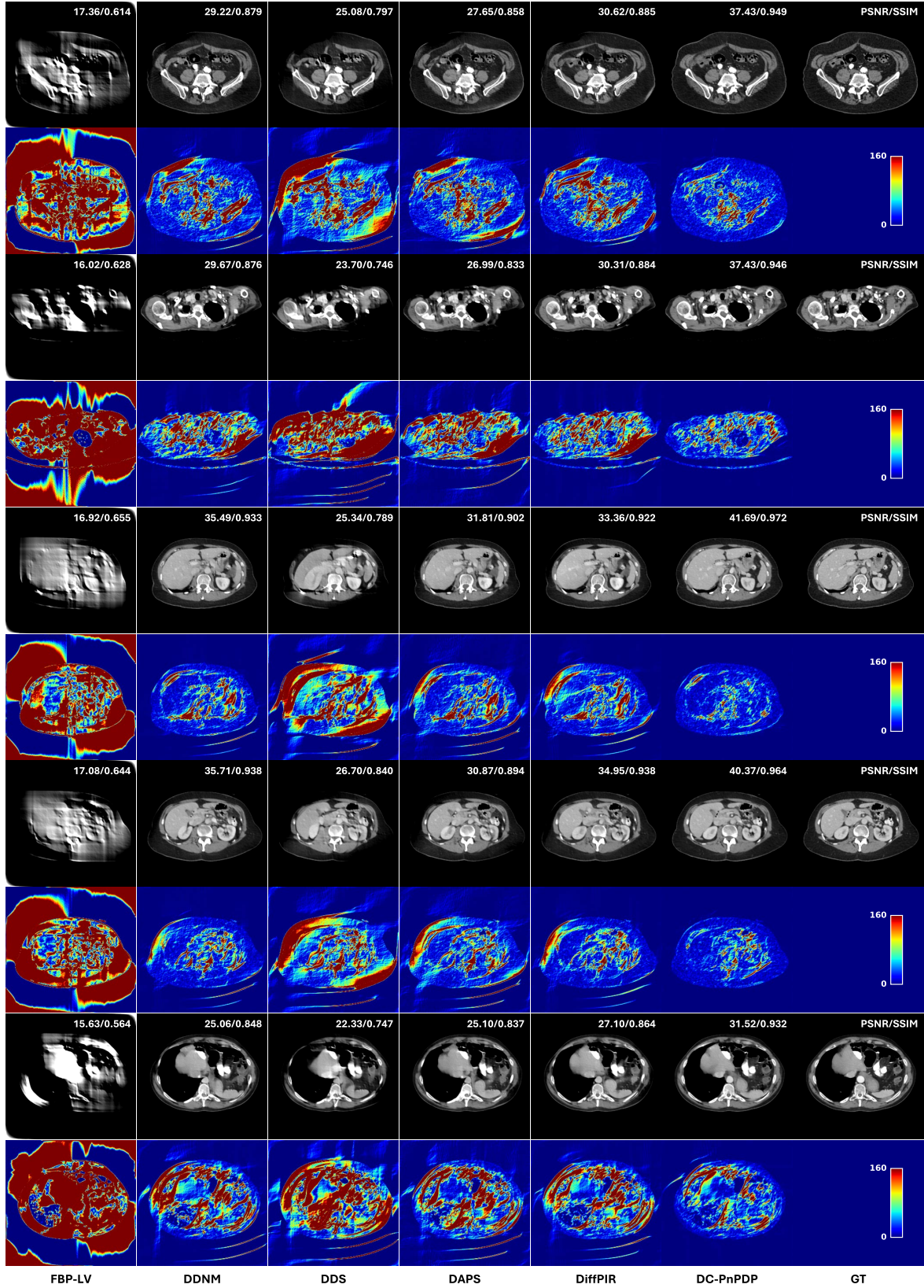


Figure 6. Qualitative comparisons on LACT of  $[0, 90]^\circ$  reconstruction tasks. Visualization windows are set to  $[-150, 250]$  HU.

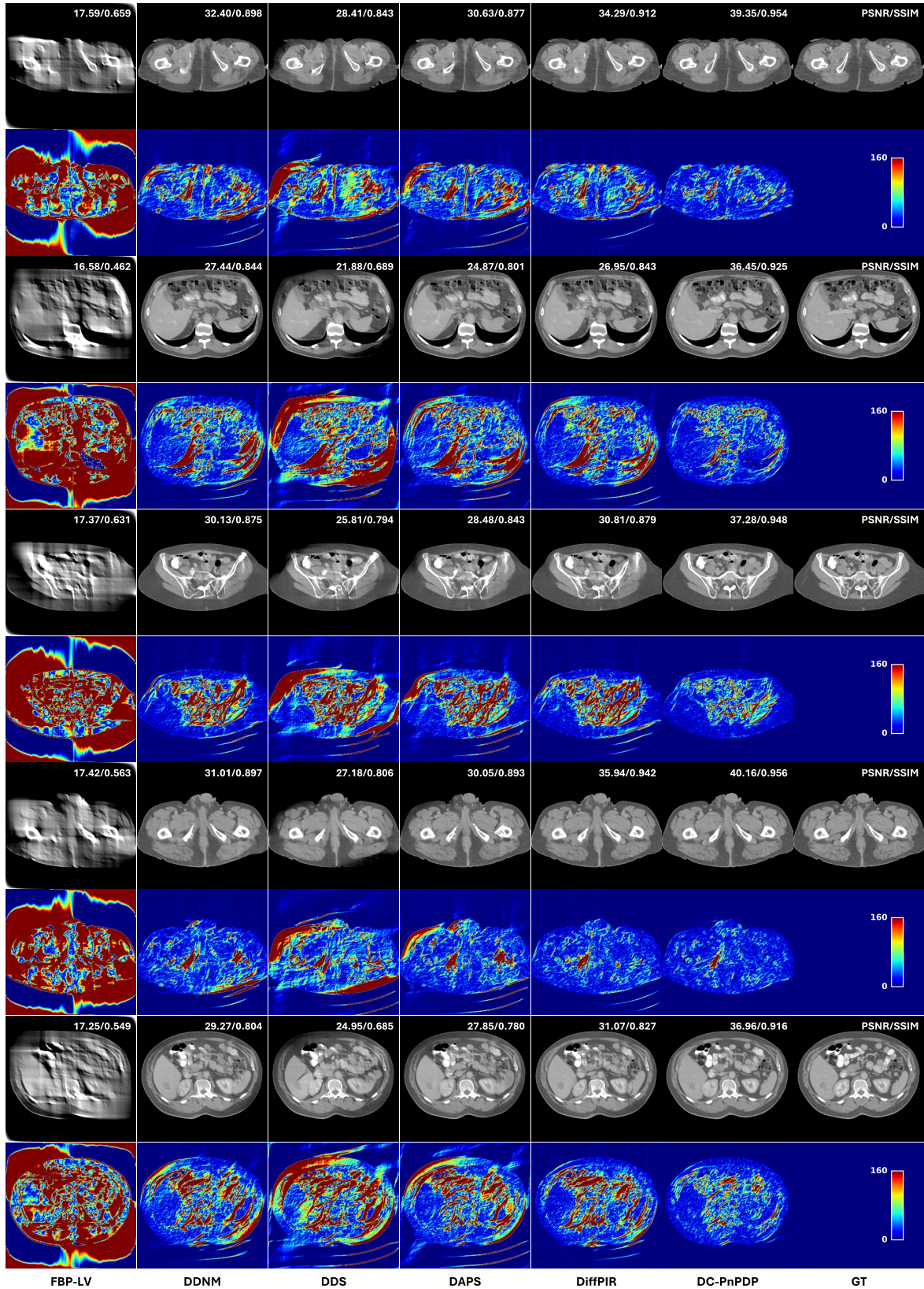


Figure 7. Qualitative comparisons on LACT of  $[0, 90]^\circ$  reconstruction tasks. Visualization windows are set to  $[-300, 300]$  HU.

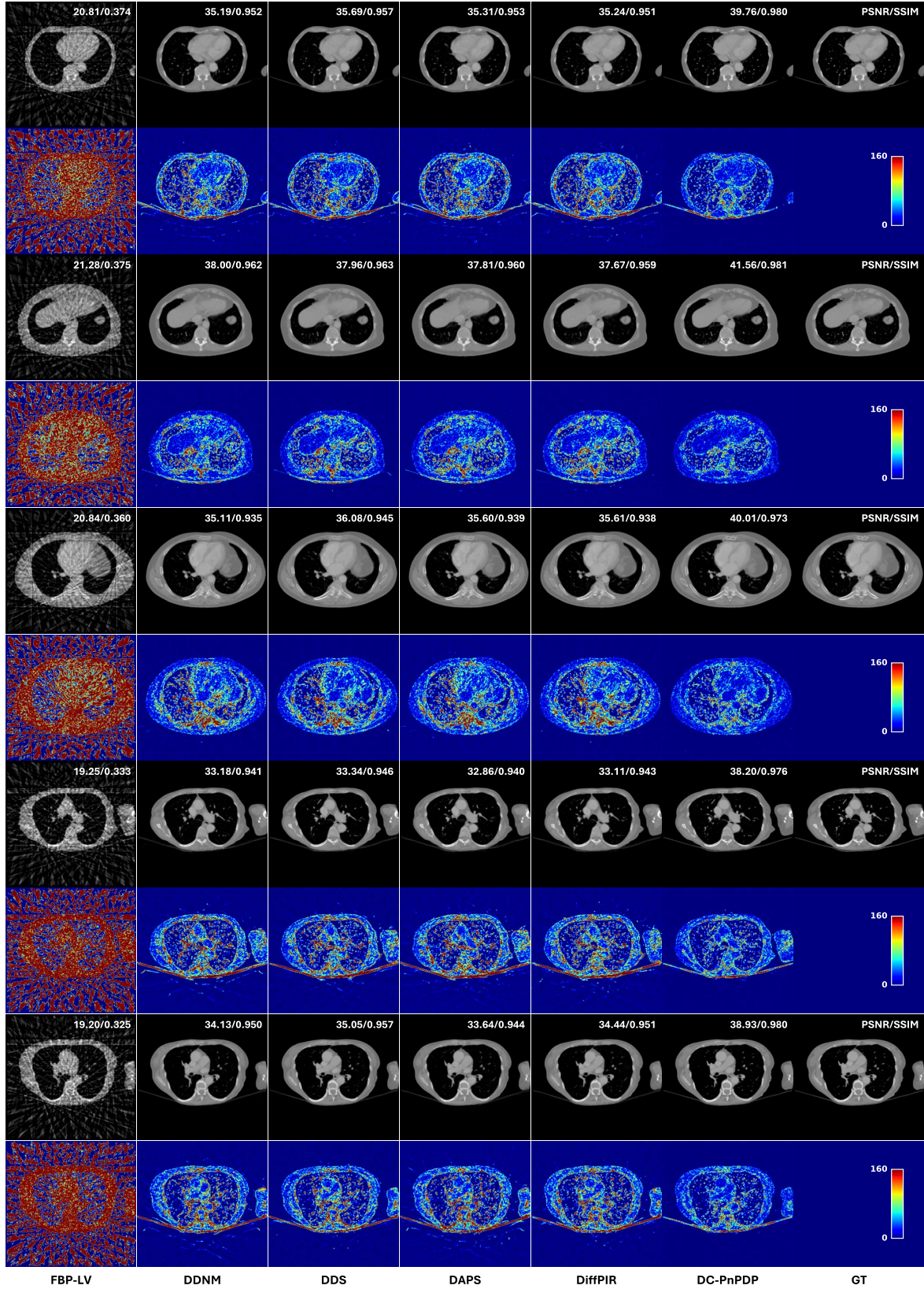


Figure 8. Qualitative comparisons on SVCT of 20 views reconstruction tasks. Visualization windows are set to  $[-800, 800]$  HU.

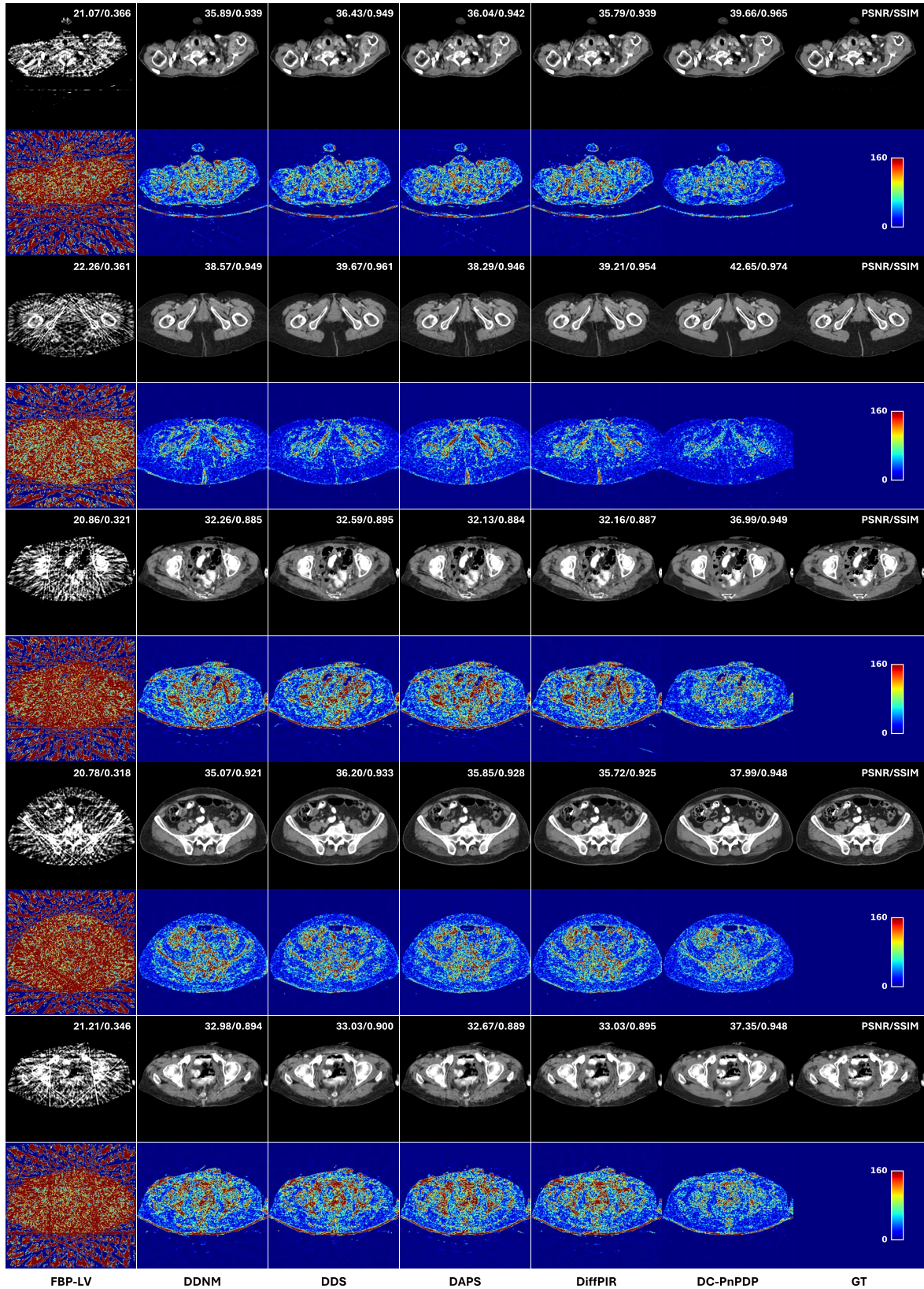


Figure 9. Qualitative comparisons on SVCT of 20 views reconstruction tasks. Visualization windows are set to  $[-150, 250]$  HU.

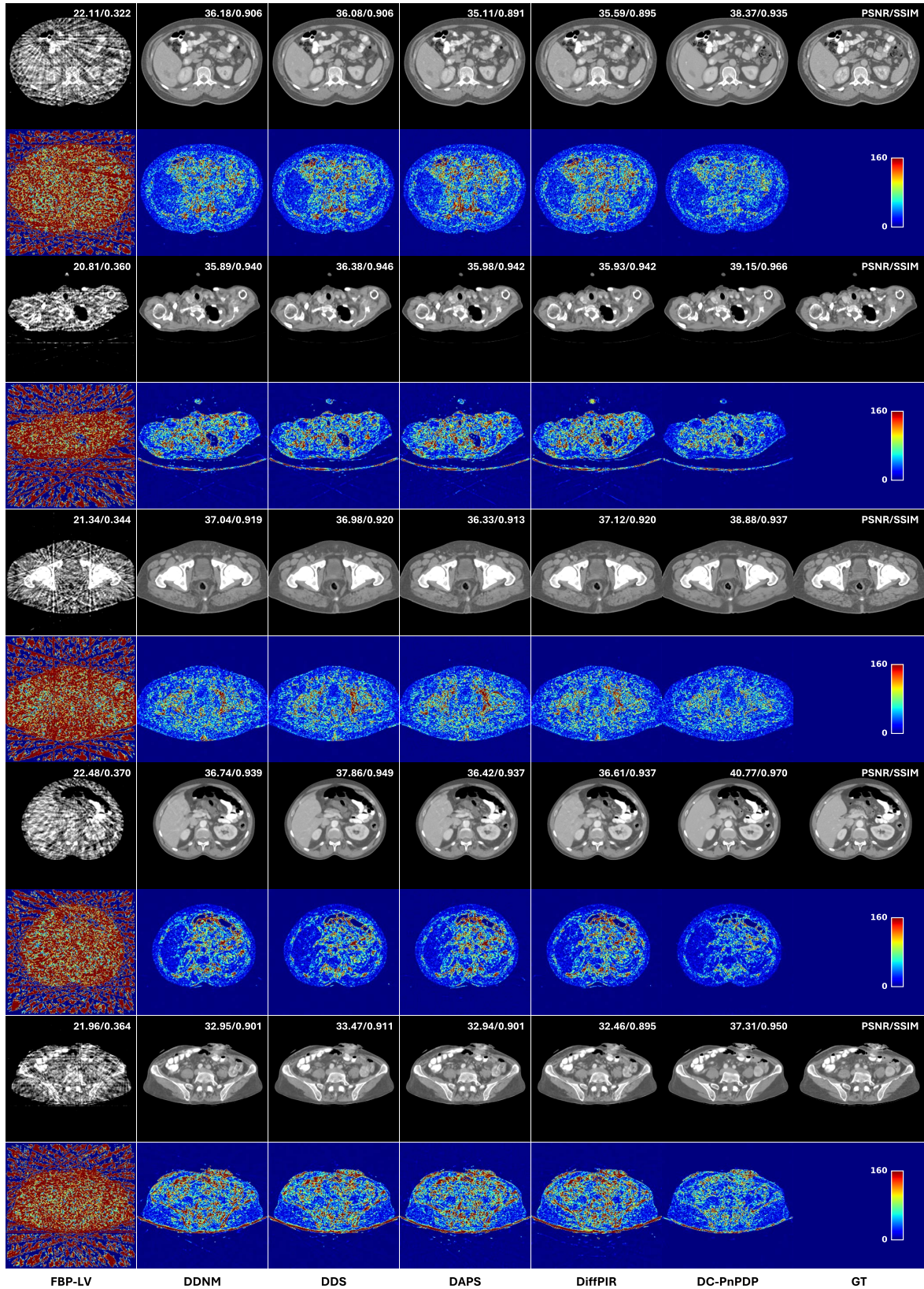


Figure 10. Qualitative comparisons on SVCT of 20 views reconstruction tasks. Visualization windows are set to  $[-300, 300]$  HU.